The Effect of Large-Scale Flow on Low-Level Frontal Structure and Evolution in Midlatitude Cyclones

DAVID M. SCHULTZ,* DANIEL KEYSER, AND LANCE F. BOSART

Department of Earth and Atmospheric Sciences, The University at Albany, State University of New York, Albany, New York

(Manuscript received 10 June 1997, in final form 10 October 1997)

ABSTRACT

Observational and modeling studies documented in the literature indicate that the large-scale flow has an important effect on the structure and evolution of low-level fronts in midlatitude cyclones. The purpose of this paper is to address the role of the large-scale flow on low-level cyclone/frontal structure and evolution through a combined observational and idealized modeling approach.

Analyses of two observed cyclone cases embedded in large-scale diffluence and confluence, respectively, are presented to illustrate two possible cyclone/frontal structures and evolutions. Specifically, the cyclone moving into a diffluent, high-amplitude ridge becomes meridionally elongated and possesses a strong meridionally oriented cold front and a weak warm front. The cold front rotates into the warm front, forming an occluded front in the manner of the Norwegian cyclone model, as indicated by the narrowing of the thermal ridge connecting the warm sector to the cyclone center. In contrast, the cyclone moving into confluent, low-amplitude zonal flow becomes zonally elongated and possesses strong zonally oriented warm and bent-back fronts and a weak cold front. The frontal structure in this case is reminiscent of the Shapiro–Keyser cyclone model, exhibiting a fracture between perpendicularly oriented cold and warm fronts (i.e., the so-called frontal T-bone structure).

The idealized simulations employ a nondivergent barotropic model in which potential temperature is treated as a passive tracer. When a circular vortex acts on an initially zonally oriented baroclinic zone, cold and warm fronts, a frontal fracture, a bent-back front, and eventually a Norwegian-like occlusion develop. When a circular vortex is placed in a diffluent background flow, the vortex and frontal zones become meridionally elongated, and the evolution resembles the Norwegian occlusion with a narrowing thermal ridge. When a circular vortex is placed in a confluent background flow, the vortex and frontal zones become zonally elongated, and the evolution resembles the Shapiro–Keyser model with a frontal fracture, frontal T-bone, and bent-back front. Although the idealized model qualitatively reproduces many of the frontal features found in the observed cyclones analyzed in the present study, one significant difference is that the maximum potential temperature gradient and frontogenesis along the cold and warm fronts may differ by a factor of 2 or more in the observed cases, but remain equal along the cold and warm fronts throughout the idealized model simulations. Possible reasons for this asymmetry in the strength of the observed cold and warm fronts are discussed.

1. Introduction

The primary paradigm by which modern synoptic meteorologists interpret midlatitude-cyclone structure and evolution is the Norwegian cyclone model, developed originally by Bjerknes (1919) and Bjerknes and Solberg (1922). Despite its success, however, subsequent research has shown that a variety of cyclone/frontal structures and evolutions are possible (e.g., Browning 1990; Shapiro and Keyser 1990; Evans et al. 1994; Smigielski and Mogil 1995; Young 1995; Bosart 1998). As a result, the Norwegian cyclone model has been criticized as being inadequate to explain the variety of low-level frontal configurations and midlatitude cyclone evolutions observed in the atmosphere (e.g., Hobbs et al. 1990, 1996; Mass 1991). Consistent with such criticisms, it has been proposed that the Norwegian cyclone model be made more flexible to allow for a broader spectrum of cyclone/frontal structures and evolutions (e.g., Sutcliffe 1952; Uccellini et al. 1992).

Recent observational and numerical modeling work indicates that the structure of individual midlatitude cyclones depends on a variety of dynamical factors: the large-scale flow (defined as the flow on scales larger than that of the cyclone and its attendant fronts) in which the cyclone is embedded (e.g., Davies et al. 1991; Thorncroft et al. 1993; Evans et al. 1994; Hartmann 1995; Wernli 1995; Young 1995), the magnitude of surface friction (land versus ocean) (e.g., Hines and Mechoso 1993; Kuo and Low-Nam 1994; Thompson 1995; Rotunno et al. 1996), diabatic heating (e.g., Nuss and Anthes 1987), and physiography (e.g., Palmén and New-

* Current affiliation: NOAA/National Severe Storms Laboratory, Norman, Oklahoma.

Corresponding author address: David M. Schultz, NOAA/National Severe Storms Laboratory, 1313 Halley Circle, Norman, OK 73069. E-mail: schultz@nssl.noaa.gov

ton 1969, section 11.8; Hobbs et al. 1990; Tibaldi et al. 1990; Steenburgh and Mass 1994; Hoffman 1995). Therefore, the Norwegian cyclone model may be most applicable to the large-scale flow regimes and physiography characteristic of the eastern North Atlantic Ocean and western Europe, the region where the model was originally developed.

Despite these criticisms and limitations, the Norwegian cyclone model still retains its popularity among operational and research meteorologists, in part because a more versatile conceptual model accounting for the broad spectrum of possible frontal structures and evolutions has yet to be proposed. Although the dynamical mechanisms for cyclogenesis may be similar over a wide distribution of observed events, the factors that account for structural and evolutionary differences between individual cyclones have not yet been comprehensively addressed. The purpose of this paper is to examine the effects of one such factor, the large-scale flow, on the low-level frontal structure and evolution of midlatitude cyclones through both case studies of observed cyclones and idealized numerical simulations of vortices. These observed cyclones and idealized model simulations are then compared to extant conceptual models of cyclone/frontal structure and evolution in order to relate our results to previous work.

In section 2 of this paper, previous literature attributing observed cyclone/frontal structure and evolution to the large-scale flow is reviewed. Also, two well-known conceptual models of cyclone/frontal structure and evolution are discussed: the Norwegian and Shapiro–Keyser (1990) models. These two models exhibit characteristic differences from each other and, as such, may be thought of as representing two realizations on a spectrum of possible cyclone evolutions. In section 3, two observed cyclone cases are presented and compared, each representing one of the conceptual models discussed previously. The case resembling the Norwegian cyclone model developed in large-scale diffluence, whereas the case resembling the Shapiro–Keyser model developed in large-scale confluence. In section 4, the observed cyclones are abstracted to a nondivergent barotropic framework by placing an idealized vortex in various background flows with potential temperature treated as a passive tracer. The evolution of an initially zonally oriented frontal zone is examined first for an isolated circular vortex in the absence of background flow, and then for an initially circular vortex placed in diffluent and confluent background flows. The resulting frontal evolutions in these simulations are compared to those of the respective observed cyclone cases and their associated conceptual models. Finally, this study is concluded in section 5.

2. Previous literature

In section 2a, a review of previous observational literature indicates a relationship between the large-scale flow and the resulting structure and evolution of fronts and cyclones, suggesting two possible realizations of cyclone structure in the atmosphere. These realizations resemble the Norwegian and Shapiro–Keyser cyclone models. Section 2b then discusses the extent to which idealized channel models of baroclinic development are consistent with these two conceptual models.

a. Observational evidence relating cyclone/frontal structure and evolution to the large-scale flow

Perhaps the earliest indication of the existence of a relationship between cyclone/frontal structure and the large-scale flow arose from research conducted during the late 1940s to early 1950s to improve long-range weather forecasting. In searching for repeatable patterns of jet-stream evolution, the concept of an index cycle was proposed (e.g., Rossby and Willett 1948; Namias 1950). Briefly, the index cycle is based on a putative oscillation in the zonal index (Rossby and Collaborators 1939) in which the jet stream evolves through several stages, ranging from a state of weak westerlies in a high-amplitude planetary wave pattern (low zonal index) to a state of strong westerlies in a low-amplitude planetary wave pattern (high zonal index) and back again. The jet stream during a period of low zonal index is characterized by cutoff cyclones and blocking anticyclones, whereas the jet stream during a period of high zonal index is characterized by relatively strong, straight zonal flow with relatively long-wavelength planetary-scale waves.

The relevance of the zonal index to the present work is indicated by Rossby and Willett (1948, 648), who stated that periods of low zonal index are characterized by ''deep occlusion of stationary cyclones in middle latitudes, and north–south orientation of pressure cells and frontal systems [with] maximum east–west rather than north–south air mass and temperature contrasts.'' In this case, diffluent blocking patterns typically occur downstream of the cyclone, and the deformation associated with this diffluence results in meridionally elongated fronts. Meridionally elongated patterns of frontogenesis along the cold front imply the presence of thermodynamically direct secondary circulations oriented in the zonal direction, thereby favoring ascent over, and abundant precipitation along, the cold front (Saucier 1955, section 11.03).

In contrast, during periods of high zonal index ''pressure systems [are] oriented east–west,'' and possess ''maximum latitudinal temperature gradient'' (Rossby and Willett 1948, 648). Saucier (1955, section 11.03) added that frontal zones and precipitation patterns would extend along the path of the zonally elongated cyclones. A plausible interpretation of these statements is that in strongly confluent flow, characteristic of entrance regions of strong jet streams, warm fronts (regions of maximum latitudinal temperature gradient) would tend to be stronger than cold fronts. Furthermore, deforma-

tion in the jet entrance region would favor patterns of frontogenesis elongated in the zonal direction, implying the presence of thermodynamically direct secondary circulations oriented in the meridional direction, associated with ascent over, and precipitation poleward of, the warm front.

The essence of these ideas also was stated by Sawyer (1950). While examining the development of secondary cyclones, he noted that occluded cyclones with strong cold fronts (cold occlusions) tend to occur within a diffluent thermal wind field (which he later argued occurs within a jet stream exit region). This type of cyclone structure resembles those found in low-zonal-index flow. In contrast, occluded cyclones with strong warm fronts (warm occlusions) tend to occur within a confluent thermal wind field (or a jet stream entrance region), resembling cyclones in high-zonal-index flow.

Although largely unsubstantiated by Rossby and Willett, the foregoing ideas are supported by more recent work. The complementary studies by Evans et al. (1994) and Young (1995) proposed classification schemes for the structure and evolution of midlatitude cyclones, based primarily on satellite imagery for cyclones over the North Atlantic Ocean. They found characteristic signatures in the satellite imagery and kinematical fields for various configurations of the large-scale flow (e.g., confluent, diffluent, high-amplitude, zonal) and for various horizontal interactions between precursors to surface cyclogenesis. The results of these two studies suggest that surface cyclones (and their attendant cloud patterns) embedded in large-scale diffluence tend to be meridionally elongated, favoring strong cold fronts (e.g., Young 1995, 252), whereas cyclones embedded in large-scale confluence tend to be zonally elongated, favoring strong warm fronts (e.g., Young 1995, 267). Smigielski and Mogil (1995) devised an objective scheme for determining central surface pressures from satellite imagery for poleward- and eastward-moving cyclones over the North Pacific Ocean. They noted that eastward-moving cyclones tend to be more zonally elongated and are more likely to be found over the western North Pacific Ocean (the confluent jet entrance region) compared to their poleward-moving counterparts (Smigielski and Mogil 1995, 881). This difference apparently is related to the stronger upper-level westerly winds that tend to be found over the western North Pacific Ocean compared to the eastern North Pacific Ocean, consistent with the results of Rossby and Willett (1948). Finally, Hartmann (1995) noted that when the Southern Hemisphere wintertime, planetary-scale 500-hPa flow is characterized by relatively weak winds with broad, bimodal jet maxima at 25° and 55°S, the cyclones tend to be meridionally elongated, but when the flow is characterized by strong winds centered around 40°S, the resulting cyclones tend to be more zonally elongated, reminiscent of the findings of Rossby and Willett (1948).

These previous results relating the structure and evolution of observed cyclones and fronts to the large-scale flow suggest two contrasting realizations of cyclone/frontal structure: (a) meridionally elongated cyclones with the cold front dominant and (b) zonally elongated cyclones with the warm front dominant. These cyclone/frontal structures are shown herein to resemble the Norwegian and Shapiro–Keyser cyclone models, respectively.

1) THE NORWEGIAN CYCLONE MODEL

The Norwegian cyclone model[1] was formulated originally as a static conceptualization without consideration of the cyclone life cycle: an open-wave cyclone with a cold and a warm front (Bjerknes 1919). Later Bergeron recognized that the area of the warm sector decreases with time and that the cold and warm fronts eventually merge, forming an occluded front (e.g., Bergeron 1959, 457; Friedman 1989, 212). Consequently, the Norwegian cyclone model was revised to allow the cyclone and its attendant fronts to evolve through a life cycle (Bjerknes and Solberg 1922).

The life cycle of a Bjerknes and Solberg (1922) cyclone, hereafter the *Norwegian cyclone model*, begins with a small-amplitude disturbance on the polar front. This disturbance consists of a cyclonic circulation that advects cold air equatorward west of the cyclone center and warm air poleward east of the cyclone center, forming cold and warm fronts, respectively. Since the cold front is observed to rotate around the system faster than the warm front, the cold front eventually catches up to the warm front, forming an occluded front. Originally Bjerknes and Solberg (1922) believed that this catch-up initially would occur away from the low center,[2] but this conceptualization would be supplanted by one where the warm sector closes from the low center outward, analogous to a zipper (Reichelderfer 1932, 31). The occluded front is identified by a thermal ridge extending from the peak of the warm sector poleward toward the low center (e.g., Mass and Schultz 1993, their Fig. 12: 30 and 33 h). Schematic illustrations of the Norwegian cyclone model usually show a strong cold front and a weaker warm front, both of which become more meridionally oriented with time (e.g., Bjerknes and Solberg 1922, 5; Petterssen 1956, 218, 231; Godske et al. 1957, 532, 536; Palmén and Newton 1969,

[1] The synthesis of the Norwegian cyclone model is examined in many reviews (e.g., Bergeron 1959; Palmén and Newton 1969, chap. 5; Kutzbach 1979, 201–220; Jewell 1981; Namias 1983; Friedman 1989; Eliassen 1994; Newton and Rodebush Newton 1994).

[2] As noted by Brunt (1934, 312), the Bjerknes and Solberg (1922) mechanism of catch-up that first occurs at a point away from the low center was related to the cyclone impacting the Skagerak peninsula of Scandinavia. This impact would slow the warm front and allow the cold front to catch up, forming an orographic occlusion (Huschke 1959, 406). We speculate that the formulation of Bjerknes and Solberg's (1922) cyclone model was influenced by this commonly observed evolution.

326), much like the meridionally elongated cyclones described in the previous section [e.g., cyclones in low-zonal-index flow (Rossby and Willett 1948; Hartmann 1995), cyclones in diffluent flow (Young 1995, 252), and poleward-moving cyclones (Smigielski and Mogil 1995)].

2) THE SHAPIRO–KEYSER (1990) CYCLONE MODEL

In an attempt to reconcile analyses of observed data obtained during field programs to study rapidly developing oceanic cyclones, numerical simulations of real cyclones, and idealized simulations of unstable baroclinic waves, Shapiro and Keyser (1990, Fig. 10.27) formulated a new conceptual model, the *Shapiro–Keyser model.* The life cycle of a Shapiro–Keyser cyclone begins as a small-amplitude disturbance on a broad low-level baroclinic zone. As the cyclone intensifies, the baroclinic zone undergoes scale contraction, forming fronts. Unlike a Norwegian cyclone, where the cold front catches up to the warm front, the cold front in a Shapiro–Keyser cyclone moves nearly perpendicular to the warm front (the *frontal T-bone*) and a weakness (*fracture*) appears in the magnitude of the horizontal temperature gradient along the poleward portion of the cold front near the low center. The frontal fracture was noted previously by Godske et al. (1957, 536) as a region of frontolysis, which they associated with lower-tropospheric subsidence. Although Godske et al. (1957) did not elaborate further on the relationship between descent and frontal fracture, we infer that the low-level horizontal divergence associated with the subsidence in this region is responsible for frontolysis. There is also the possibility that differential adiabatic warming may weaken the low-level horizontal temperature gradient, a factor that can only apply above the surface in the absence of topography. Although subsidence leading to frontolysis in this region may be consistent with the formation of the fracture, it will be shown in section 4b that the differential rotation of isentropes can lead to fracturing in the absence of vertical motion.

Next, air parcels in the warm-frontal zone of a Shapiro–Keyser cyclone transport their baroclinicity west of the cyclone center, a process discussed by Takayabu (1986) in an idealized channel model simulation of baroclinic waves. The resulting feature, previously identified by Bjerknes (1930) and referred to as a *retrograde occlusion* by Bergeron (1937) [later called the *back-bent, loop, broken-back, or bent-back occlusion* (e.g., Bergeron 1937; Huschke 1959, 65)], was termed a *bent-back warm front* by Shapiro and Keyser (1990), hereafter a *bent-back front.*[3] The strong zonally oriented baroclinicity along the warm and bent-back fronts and the weakening of the poleward portion of the cold front result in the zonal elongation of the fronts, distinctly different from the meridional elongation of the fronts in the Norwegian cyclone model. The zonal elongation characteristic of the Shapiro–Keyser cyclone model is consistent with observations of zonally elongated cyclones discussed in the previous section [e.g., cyclones in high-zonal-index flow (Rossby and Willett 1948; Hartmann 1995), cyclones in confluent flow (Young 1995, 267), and eastward-moving cyclones (Smigielski and Mogil 1995)].

Finally, the bent-back front wraps around the low center, enclosing a pool of relatively warmer air and forming a *warm-core seclusion,* or simply *warm seclusion.* For a numerical simulation of a cyclone over the western North Atlantic Ocean, Kuo et al. (1992) showed that the air inside the seclusion originates in the warm-frontal zone ahead of the storm and this air is encircled by more rapidly moving colder air originating farther poleward. Note that the formation of the warm seclusion differs from the Norwegian occlusion process because the cold and warm fronts are nearly perpendicular to each other during the frontal T-bone stage of a Shapiro–Keyser cyclone; therefore, the Norwegian occlusion process of the catch-up of the warm front by the cold front does not occur. Nevertheless, as noted by Shapiro and Donall Grell (1994) and Thompson (1995), some cyclones that possess the characteristics of Shapiro–Keyser cyclones (i.e., frontal fracture, bent-back front, and frontal T-bone) early in their life cycle can develop a Norwegian-like occlusion later in their life cycle as the warm sector eventually narrows and the cyclone becomes more meridionally elongated. For the purposes of this paper, we consider a Shapiro–Keyser cyclone to be one in which a Norwegian-like occlusion does not form, but rather the cold and warm fronts maintain a nearly perpendicular orientation throughout the life cycle of the cyclone.

b. Modeling evidence relating cyclone/frontal structure and evolution to the large-scale flow

As discussed in the previous section, observational studies reveal the existence of two distinct conceptual models of cyclone/frontal structure and evolution and suggest that the distinction between them may be attributed to characteristic differences in the large-scale flow. In this section, modeling evidence for this hypothesis is examined.

Idealized channel models of baroclinic development have been important tools for understanding cyclogenesis, and numerical experiments have indicated that the cyclone/frontal structures simulated in these models are very sensitive to the specification of the basic state (e.g., Hoskins and West 1979; James 1987; Davies et al. 1991; Thorncroft et al. 1993). For example, Hoskins and West (1979) performed a suite of three-dimensional semi-

[3] Because cold advection can occur in association with bent-back warm fronts [e.g., as noted in observational studies of oceanic cyclones (Shapiro and Keyser 1990; Neiman and Shapiro 1993; Blier and Wakimoto 1995), numerical modeling studies of oceanic cyclones (Kuo et al. 1991, 1992; Reed et al. 1994), and an idealized channel-model study of baroclinic development (Hoskins 1983, 18)], we refer to bent-back warm fronts as *bent-back fronts.*

geostrophic channel model simulations in which the basic state is varied from the meridionally independent, vertically sheared zonal flow of the Eady (1949) model to a parabolic jet profile in the meridional direction. As the basic-state zonal flow varies from the Eady specification to the jet profile, the structure of cyclones arising from the finite-amplitude development of unstable normal modes varies from a preferred meridional orientation to a more isotropic configuration.

Another demonstration of the relationship between the cyclone/frontal structure and the large-scale flow entails the addition of cyclonic or anticyclonic barotropic shear to the basic state. For example, Davies et al. (1991) found that by adding cyclonic barotropic shear to a westerly basic-state jet, growing normal modes in a semigeostrophic channel model produce stronger warm fronts, become more zonally elongated, occlude more rapidly, and feature lower central surface pressures than normal modes growing in the basic state excluding barotropic shear. On the other hand, growing normal modes in a westerly basic-state jet incorporating anticyclonic barotropic shear develop longer, stronger cold fronts, become more meridionally elongated, occlude more slowly, and feature higher central surface pressures than normal modes growing in the basic state excluding barotropic shear. Wernli (1995) obtained similar results when conducting the same experiments for a zonally isolated cyclone in a semigeostrophic channel model. Using a primitive equation channel model in spherical coordinates, Hoskins (1983, 1990) and Thorncroft et al. (1993) also showed that the evolution of cyclones from unstable normal modes may be altered by introducing barotropic shear to the basic-state zonal flow. For example, Thorncroft et al. (1993) considered the life cycles of cyclones embedded in two basic-state zonal flows: LC1 (basic state with no barotropic shear) and LC2 (basic state with cyclonic barotropic shear). LC1 cyclones become meridionally elongated with long, strong cold fronts, whereas LC2 cyclones are more isotropic with strong warm fronts, results that qualitatively resemble those of Davies et al. (1991) and Wernli (1995).

Although these simulations indicate that the large-scale flow is important in modulating the resulting cyclone/frontal structure and evolution, there are limitations to applying these results to the observed conceptual models discussed previously. In the case of the anticyclonic-shear simulations of Davies et al. (1991) and Wernli (1995), whereas some aspects of the Norwegian cyclone model develop in the resulting cyclones (e.g., meridional elongation, strong cold fronts), other aspects do not appear systematically (i.e., the cold front and the warm front remain nearly perpendicular to each other so that a Norwegian occlusion does not occur). This evolution is so unusual that Wernli (1995, 56) questions whether the anticyclonic-shear case has a counterpart in the real atmosphere. On the other hand, the addition of cyclonic barotropic shear to these simulations tends to result in the formation of zonally elongated cyclones with strong warm fronts, but other aspects of the Shapiro–Keyser model do not appear systematically. For example, although the cyclonic-shear simulation in Davies et al. (1991) and LC2 in Thorncroft et al. (1993) develop a well-defined frontal T-bone, the cyclonic-shear simulation in Wernli (1995) develops a Norwegian-like thermal ridge. The foregoing discussion suggests that modeling studies in which the basic-state barotropic shear is varied, although useful as a first step in understanding the dependence of cyclone/frontal structures on the large-scale flow, have limited success in reproducing the Norwegian and Shapiro–Keyser cyclone/frontal conceptual models. It is hypothesized that this limitation of the aforementioned modeling studies arises in part from the lack of consideration of more realistic, longitudinally varying basic states, a factor recognized as being important to the resulting cyclone/frontal structure and evolution from the observational studies described in section 2a and the observed cases to be presented in section 3. As will be shown in section 4, idealized model simulations with background diffluence and confluence are capable of yielding the desired evolutions.

Another factor that has been proposed to explain the differences between Norwegian and Shapiro–Keyser cyclones and that has been tested using numerical models is the magnitude of surface friction (land versus ocean). Since Norwegian (Shapiro–Keyser) cyclones had been predominantly observed over land (ocean), it was speculated that the magnitude of surface friction plays a role in distinguishing between these characteristic cyclone/frontal evolutions (e.g., Mass 1991, 352; Hines and Mechoso 1993; Mass and Schultz 1993, 914). To test this hypothesis, modeling studies were performed where the magnitude of surface friction is varied for real (Kuo and Low-Nam 1994) and idealized (Hines and Mechoso 1993; Thompson 1995; Rotunno et al. 1996) cyclones. For example, Hines and Mechoso (1993) considered the evolution of growing normal modes in a primitive equation channel model for three different values of the surface-drag coefficient, referred to as the no-drag, ocean-drag, and land-drag simulations. Hines and Mechoso (1993) confirm that fewer Shapiro–Keyser-like features (frontal fracture, bent-back front, warm seclusion) develop in the land-drag simulation. One aspect inconsistent with their hypothesis is that the cold and warm fronts in the land-drag case are still nearly perpendicular (Hines and Mechoso 1993, Fig. 5), a characteristic more closely resembling the frontal T-bone in the Shapiro–Keyser model rather than the narrowing warm sector in the Norwegian cyclone model. Therefore, although the magnitude of surface friction can alter the structure of cyclones, this factor taken alone cannot account for the differences between the Norwegian and Shapiro–Keyser conceptual models.

3. Observed cyclone events

The outcome of the previous section suggests that differences in the characteristic structures and evolutions of Norwegian and Shapiro–Keyser cyclones may be attributed to the background flow in which each cyclone is embedded. This inference is examined in the present section by comparing two observed cases resembling these respective conceptual models.

a. Methodology

To bound the scope of the forthcoming comparison, two criteria are adopted for the selection of the observed cyclone cases. First, in order to reduce the direct effects of topography and variations in surface friction, only oceanic cyclones are considered. Second, only mobile midlatitude cyclones are examined, eliminating stationary cyclones (e.g., incipient lee cyclones), polar lows, and tropical cyclones. With these criteria in mind, the National Centers for Environmental Prediction's (NCEP) North Atlantic surface analyses for two periods [December 1988–February 1989: the Experiment on Rapidly Intensifying Cyclones over the Atlantic (ERICA; Hadlock and Kreitzberg 1988); January 1993–April 1993] were examined subjectively for cyclones that possessed characteristics most closely resembling those of the Norwegian and Shapiro–Keyser cyclone models. These two periods were selected on the basis of expediency with regard to the availability of data. The two resulting cases are described in sections 3b(1) and 3b(2), respectively.

To select a gridded dataset for these two cyclones, we invoke the following requirements. First, to ensure adequate data coverage and to maintain consistent data quality among the two cyclone cases, particularly over the relatively data-sparse North Atlantic Ocean, a global dataset is necessary. Second, frontal systems and features represented in derived quantities such as vorticity and frontogenesis must have temporal continuity. Third, because we are interested in comparing the synoptic- and meso-α-scale [as defined by Orlanski (1975)] features of the fronts, namely, their shape and intensity, between the two conceptual models, the dataset must resolve these features and the larger-scale frontal environment, even if it cannot resolve explicitly smaller-scale aspects of the fronts themselves.

The European Centre for Medium-Range Weather Forecasts (ECMWF) uninitialized analyses (Trenberth 1992) satisfy our requirements and are adopted for the present comparison. The ECMWF analyses are useful in a variety of contexts, including planetary- and synoptic-scale studies of midlatitude cyclone/frontal systems, as has been demonstrated previously by a number of authors (e.g., Cammas and Ramond 1989; Ayrault et al. 1995; Bosart et al. 1996; Schultz et al. 1997; Wernli and Davies 1997; Lackmann et al. 1997). The 6-h ECMWF analyses include all mandatory levels up to 10 hPa and are stored in spherical harmonic form at a spectral truncation of T106, which corresponds to a horizontal resolution of 1.125° latitude × 1.125° longitude, but the data are bilinearly interpolated to a 1° × 1° grid for computational convenience. All gridded data are stored, analyzed, and displayed using the Generalized Meteorological Analysis Package (GEMPAK; Koch et al. 1983).

In order to compare the observed cyclone cases presented later in this section to the idealized model simulations presented in section 4, we desire to separate the components of the observed flow fields into portions attributable to the disturbance (nominally, the cyclone and its fronts) and the background (the portion of the flow remaining following extraction of the cyclone and its fronts). The Lanczos (1956) temporal filter as described by Duchon (1979) and implemented by Lackmann et al. (1997, appendix) is adopted here. An important property of the Lanczos filter is that the half-power period (the period that partitions the spectral power equally between the high- and low-pass components) can be selected independently of the number of weights (equivalent to the number of observations in the time series). This property is advantageous because the two observed cyclones each require a different half-power period (120 h versus 360 h), since one cyclone [case ATL1 in section 3b(1)] moved more rapidly than the other [case IOP8 in section 3b(2)]. Because the sharpness of the response function decreases for longer half-power periods for a fixed number of weights (Duchon 1979, Figs. 3 and 4), preliminary tests were conducted to determine the number of weights required for half-power periods of 120 and 360 h, with this number reflecting a trade-off between data storage limitations and the sharpness of the response function. Accordingly, 241 weights for the 120-h Lanczos filter and 481 weights for the 360-h filter are chosen. For the 6-h ECMWF analyses, the 241- (481-) weight filter requires 30 (60) days of data on either side of the central time. The response functions for the two low-pass filters used in this study are displayed in Fig. 1. (The high-pass-filtered fields are obtained by subtracting the low-pass-filtered fields from the total fields.) As a consequence of its shorter half-power period, the 241-weight 120-h filter (Fig. 1a) possesses a sharper response between the high- and low-pass periods than the 481-weight 360-h filter (Fig. 1b).

In order to diagnose where the horizontal flow is conducive to frontogenesis or frontolysis, we calculate frontogenesis as defined by Petterssen (1936) for adiabatic, horizontal flow. Frontogenesis, F, is defined as the Lagrangian rate of change of the magnitude of the horizontal gradient of potential temperature θ:

$$F = \frac{d}{dt}|\nabla_p \theta|, \tag{1}$$

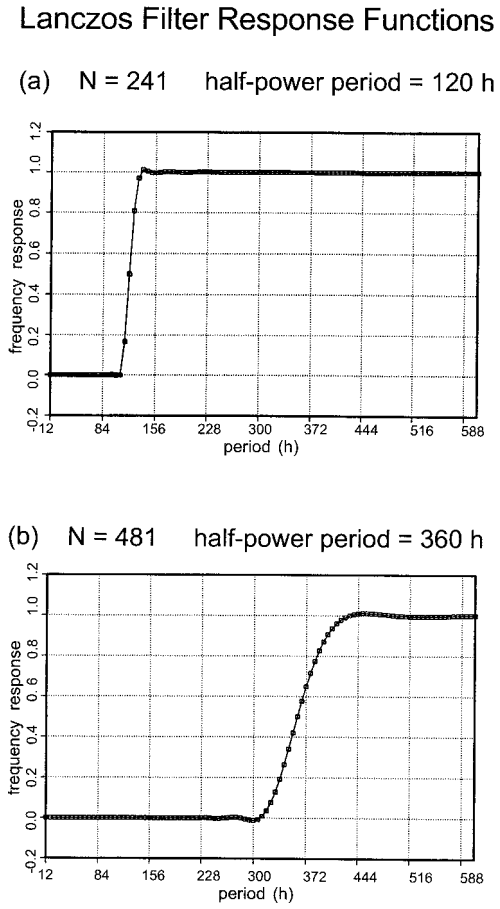

FIG. 1. Response functions for the low-pass Lanczos filters used in this paper: (a) 241-weight filter with a 120-h half-power period; (b) 481-weight filter with a 360-h half-power period.

where

$$\frac{d}{dt} = \frac{\partial}{\partial t} + u\frac{\partial}{\partial x_p} + v\frac{\partial}{\partial y_p},$$

$$\nabla_p = \mathbf{i}\frac{\partial}{\partial x_p} + \mathbf{j}\frac{\partial}{\partial y_p},$$

and $\mathbf{V} = (u, v)$ is the horizontal velocity. The subscript p indicates differentiation on an isobaric surface and hereafter will be implicit in this section.

To facilitate direct comparison between the observed cases in this section and the idealized model simulations in section 4, we adopt the expression for frontogenesis derived originally by Petterssen (1936, 10; 1956, 202). Petterssen showed that, assuming conservation of potential temperature and neglecting vertical motion, (1) can be rewritten

$$F = \frac{1}{2}|\nabla\theta|(E\cos 2\beta - \nabla\cdot\mathbf{V}), \tag{2}$$

where β is the local angle between an isentrope and the axis of dilatation. The resultant deformation is $E = (E_{st}^2 + E_{sh}^2)^{1/2}$, where $E_{st} = \partial u/\partial x - \partial v/\partial y$ is the stretching deformation, and $E_{sh} = \partial v/\partial x + \partial u/\partial y$ is the shearing deformation. Equation (2) can be separated into parts due to deformation (F_E) and divergence (F_D):

$$F_E = \frac{1}{2}|\nabla\theta|E\cos 2\beta, \tag{3}$$

$$F_D = -\frac{1}{2}|\nabla\theta|\nabla\cdot\mathbf{V}, \tag{4}$$

such that $F = F_E + F_D$.

b. Case studies

In this section, two cases, one representing each of the conceptual models discussed in section 2a, are presented. In the first case, hereafter abbreviated ATL1 [as denoted by Schultz (1996, section 4.4)], the cyclone was embedded in large-scale diffluence and moving into a high-amplitude downstream ridge. A long, intense, meridionally elongated cold front developed, and eventually a thermal ridge resembling the Norwegian occlusion formed—the entire life cycle occurring in approximately two days. The other case, ERICA intensive observation period (IOP) 8 [documented in Hartnett et al. (1989)], hereafter abbreviated IOP8 [as denoted by Schultz (1996, section 4.3)], developed on the west side of a broad ridge at the entrance to strong large-scale confluence. A long, intense, zonally oriented warm front and Shapiro–Keyser cyclone features (frontal fracture, frontal T-bone, bent-back front) developed over a period of four days, much longer than in ATL1. This difference in timescale will be addressed in section 4c.

1) OCCLUSION OVER THE WESTERN NORTH ATLANTIC OCEAN (ATL1): 9–10 FEBRUARY 1993

The 850-hPa geopotential height and relative vorticity (hereafter, height and vorticity, respectively) for three times in the life cycle of ATL1, 12 h apart, are shown in Fig. 2. At 0000 UTC 9 February 1993 (hereafter 9/00), the vorticity maximum that eventually would develop into ATL1 was situated over southeastern Canada (Fig. 2a) and, 12 h later (9/12), was joined by a frontal wave emerging from the Carolina coast (Fig. 2b). The merger of these two vorticity maxima resulted in a meridionally elongated, comma-shaped distribution of vorticity that, in another 12 h (10/00), had moved to the northeast and strengthened as the cyclone intensified (Fig. 2c).

The 850-hPa potential temperature, axes of dilatation of the total horizontal wind, and frontogenesis [as expressed in (2)] are shown in Fig. 3. By performing our analysis of the thermal structure at 850 hPa, surface-based fronts remain relatively well-defined and diabatic effects associated with surface boundaries such as the Gulf Stream are minimized. Throughout cyclogenesis,

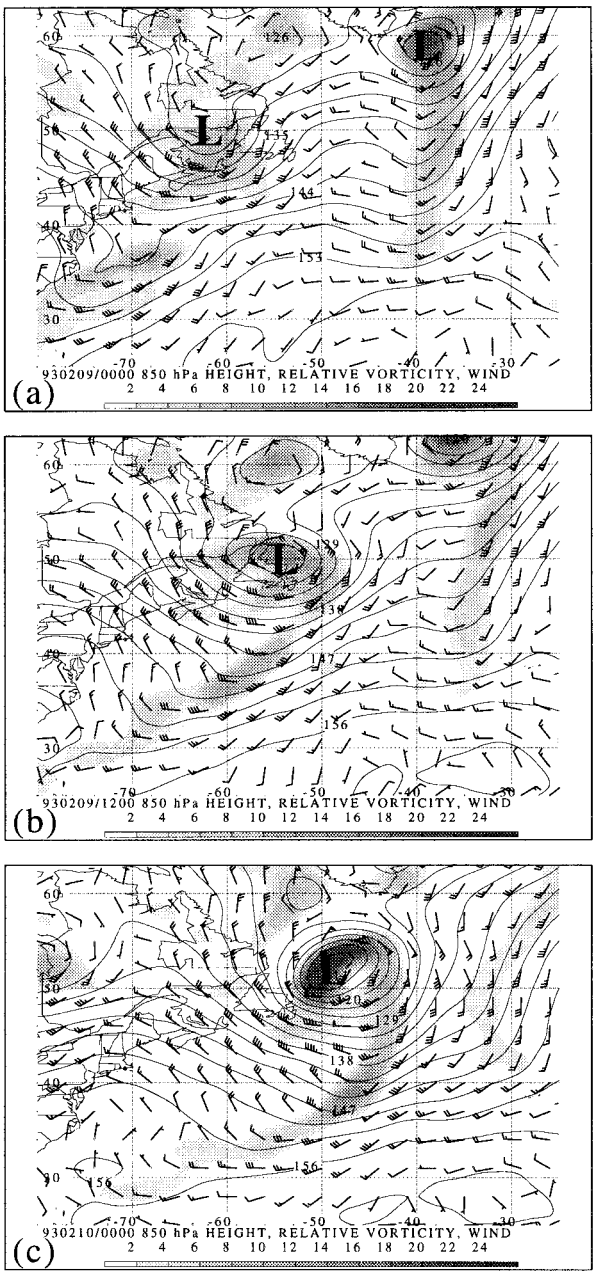

FIG. 2. ATL1 850-hPa geopotential height (solid lines every 3 dam), relative vorticity of total horizontal wind (10^{-5} s^{-1}, shaded according to scale at bottom of figure), and horizontal wind [pennant, full barb, and half-barb denote 25, 5, 2.5 m s^{-1}, respectively; separation between displayed wind vectors is 3° (every third grid point)]. Large L's indicate the locations of 850-hPa low centers. (a) 0000 UTC 9 February 1993; (b) 1200 UTC 9 February 1993; (c) 0000 UTC 10 February 1993.

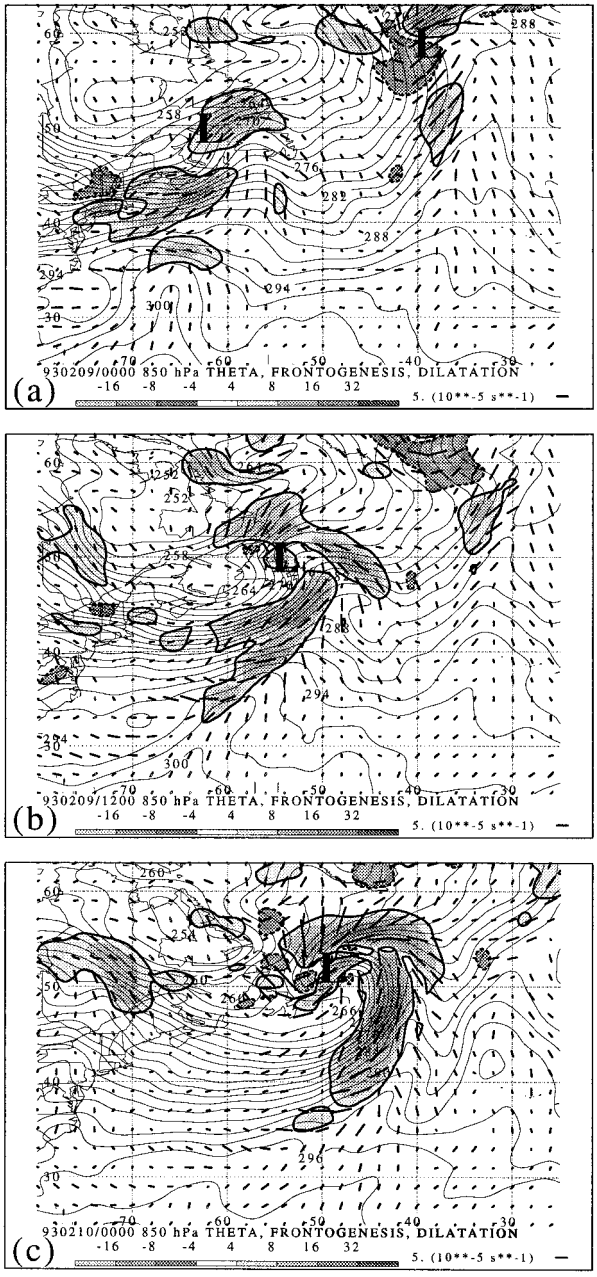

FIG. 3. ATL1 850-hPa potential temperature (thin solid lines every 2 K), frontogenesis due to total horizontal wind [10^{-1} K (100 km)$^{-1}$ (3 h)$^{-1}$, shaded according to scale at bottom of figure; solid (dashed) lines surrounding shading represent frontogenesis (frontolysis) values of 4 (-4) $\times$ 10^{-1} K (100 km)$^{-1}$ (3 h)$^{-1}$], and axes of dilatation of total horizontal wind [10^{-5} s^{-1}, scaled according to legend; separation between displayed axes of dilatation is 2° (every other grid point)]. Large L's indicate the locations of 850-hPa low centers. (a) 0000 UTC 9 February 1993; (b) 1200 UTC 9 February 1993; (c) 0000 UTC 10 February 1993.

the regions where the magnitude of the horizontal potential temperature gradient (hereafter, the potential temperature gradient) and frontogenesis were relatively large possessed greater maxima and extended over a greater area along the cold front than those along the warm front (Figs. 3a–c). At the early stages of development (9/00), the cold front extended southwestward away from the low center, while a short warm front was found to the northeast of the low center (Fig. 3a). Twelve hours later (9/12), both the cold and warm fronts had

lengthened and strengthened (Fig. 3b). By 10/00, the cold front had rotated cyclonically to the southeast side of the cyclone, catching up to the warm front (Fig. 3c). The thermal ridge that extended from the warm sector back to the cyclone center narrowed, aided by a protrusion of cold air encircling the low center from the south, producing a structure reminiscent of the Norwegian occlusion [cf. Fig. 3c and Mass and Schultz (1993, Fig. 12: 30 h)]. Despite the similarity of the frontogenesis pattern to a frontal T-bone (Fig. 3c), the lack of a frontal fracture and bent-back front, as well as the presence of the thermal ridge, dominant cold front, and meridional elongation of the cyclone, indicate a Norwegian occlusion.

The 300-hPa flow is presented in Fig. 4. Initially (9/00), the 850-hPa cyclone developed on the cyclonic-shear side of a 300-hPa jet maximum located east of Maine (Fig. 4a). The 300-hPa flow was diffluent along 40°–50°W with strong southerlies, poleward of the jet streak exit region, flowing into a high-amplitude blocking ridge, and strong northerlies equatorward of the jet streak exit region (Fig. 4a). As the cyclone developed, the trough amplified and moved slowly eastward, while the strongly diffluent, high-amplitude ridge downstream was maintained (Figs. 4b,c).

To help define the shape and scale of the flow features selected for the idealized simulations in section 4 and to show that this persistent diffluence and downstream high-amplitude ridge were characteristics of the deep-tropospheric background flow, the total 850- and 300-hPa flows are partitioned into high- and low-pass components at 9/12 and 10/00, following the procedures described in section 3a. The high-pass 850-hPa height fields at 9/12 and 10/00 indicate a low center of approximately 400-km radius intensifying from −9 to −15 dam and becoming elongated meridionally as it moved into the downstream diffluent low-pass ridge (Figs. 5a,c). The 850-hPa cyclone was located beneath the diffluent exit region of a strong 300-hPa low-pass jet maximum of about 50 m s^{-1} (Figs. 5b,d). The similarity in the shape of the 850- and 300-hPa low-pass height fields at the two displayed times suggests that the diffluence and high-amplitude ridge downstream of ATL1 are tropospheric-deep features.

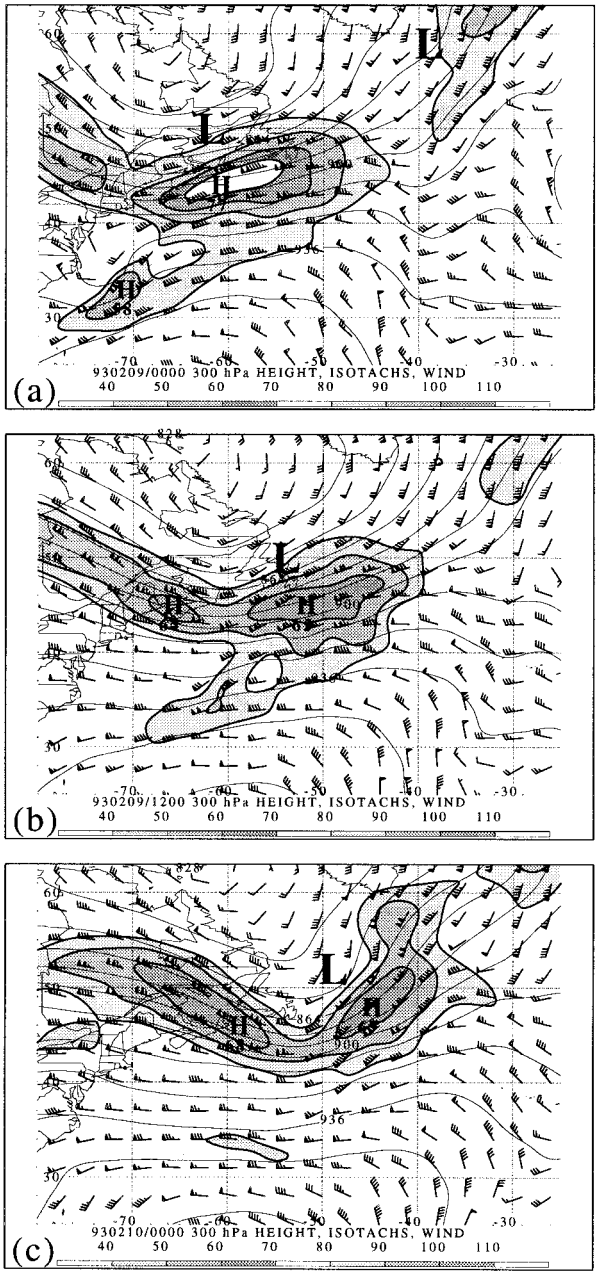

FIG. 4. ATL1 300-hPa geopotential height (thin solid lines every 12 dam), total horizontal wind speed (m s^{-1}, contoured and shaded according to scale at bottom of figure; small H's indicate the locations of wind speed maxima), and total horizontal wind [pennant, full barb, and half-barb denote 25, 5, 2.5 m s^{-1}, respectively; separation between displayed wind vectors is 3° (every third grid point)]. Large L's indicate the locations of 850-hPa low centers. (a) 0000 UTC 9 February 1993; (b) 1200 UTC 9 February 1993; (c) 0000 UTC 10 February 1993.

2) ERICA IOP 8 (IOP8): 23–26 FEBRUARY 1989

The evolution of the 850-hPa height and vorticity for IOP8 is shown every 36 h in Fig. 6. A relatively strong vorticity maximum centered over South Carolina rotated around the base of a well-defined trough over the east coast of the United States at 1200 UTC 23 February 1989 (hereafter 23/12) (Fig. 6a) and merged with a band of vorticity extending northeastward from the cyclone center along an axis of strong confluence at 25/00 (Fig. 6b). Thirty-six hours later (26/12), the cyclone moved to the northeast and became more zonally elongated as a frontal wave formed east of the primary low center at 48°N, 43°W (Fig. 6c).

The 850-hPa potential temperature and frontogenesis patterns at 23/12 (Fig. 7a) show an initially southwest–northeast elongated frontal band with the potential tem-

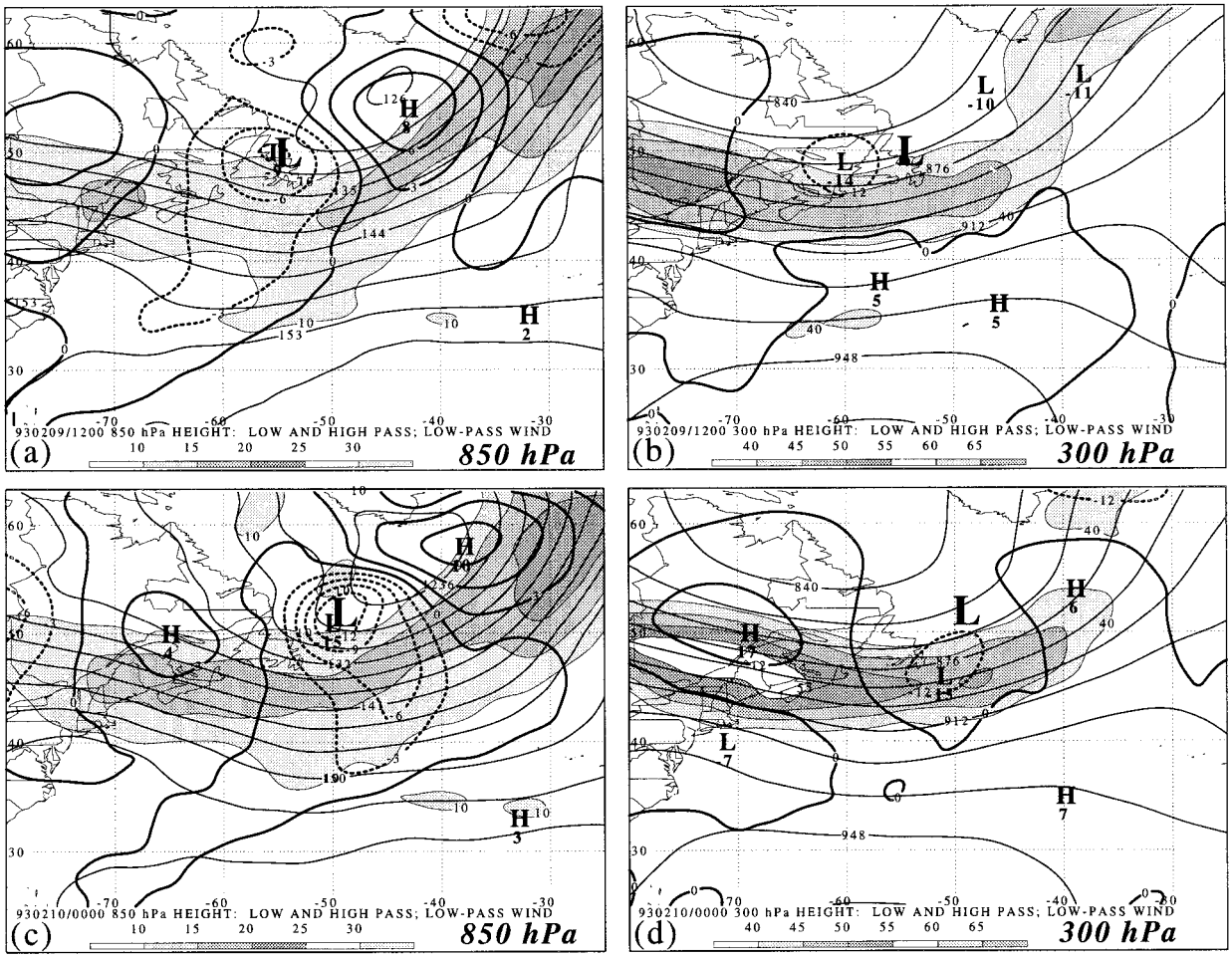

FIG. 5. ATL1 scale-partitioned fields. Large L's indicate the locations of 850-hPa low centers. (a) 850-hPa low-pass geopotential height (thin solid lines every 3 dam), 850-hPa high-pass geopotential height [thick lines every 3 dam; positive and zero (negative) values solid (dashed); small H's (L's) indicate maxima (minima)], and 850-hPa low-pass wind speed (m s^{-1}, contoured and shaded according to scale at bottom of figure) at 1200 UTC 9 February 1993. (b) 300-hPa low-pass geopotential height (thin solid lines every 12 dam), 300-hPa high-pass geopctential height [thick lines every 12 dam; positive and zero (negative) values solid (dashed); small H's (L's) indicate maxima (minima)], and 300-hPa low-pass wind speed (m s^{-1}, contoured and shaded according to scale at bottom of figure) at 1200 UTC 9 February 1993. (c) As in (a) except for 0000 UTC 10 February 1993. (d) As in (b) except for 0000 UTC 10 February 1993.

perature gradient and frontogenesis oriented northeast of the 850-hPa cyclone center (the warm front) stronger than that to the southwest (the cold front). By 25/00, the warm front became more zonally elongated and the cold front continued to weaken relative to 23/12 (Figs. 7a,b), in contrast to ATL1 where the cold front became more meridionally elongated and strengthened over time (Figs. 3a,b). The frontolysis extending southwest–northeast through the IOP8 cyclone center and the nearly 90° angle between the cold and warm fronts are reminiscent of the frontal fracture and T-bone, respectively (Fig. 7b). Finally, by 26/12, the cold front, a long broad band of baroclinicity extending from southeast of the low center to Cuba, weakened, while the warm front, east of the low center, remained strong, especially near the developing frontal wave (Fig. 7c). A region of enhanced baroclinicity resembling a bent-back front, and undergoing frontolysis, extended from the low center southwestward toward New England. The strong warm front remained nearly perpendicular to the weaker baroclinicity along the cold front, in contrast to ATL1 where the warm sector narrowed, forming a Norwegian occlusion (cf. Figs. 7c and 3c). In addition, the evolution of the frontal features in IOP8 was much slower (72 h in Figs. 7a–c) than the evolution in ATL1 (24 h in Figs. 3a–c). Note that IOP8 does not feature a warm seclusion, in contrast to the Shapiro–Keyser cyclone model. Assuming that a warm seclusion actually formed in this case, a reason for its absence might be that its horizontal scale was too small to be resolved by the ECMWF analysis. Alternatively, the baroclinicity along the bent-back front or the winds may have been too weak to produce a well-defined warm seclusion. Despite the absence of a well-defined warm se-

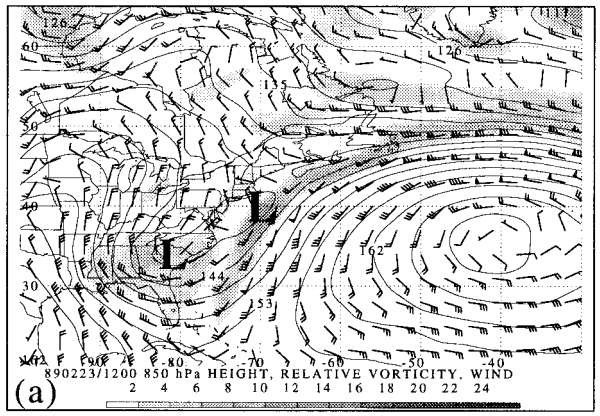

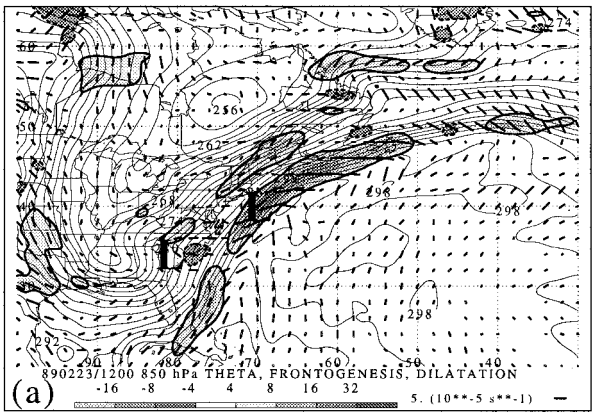

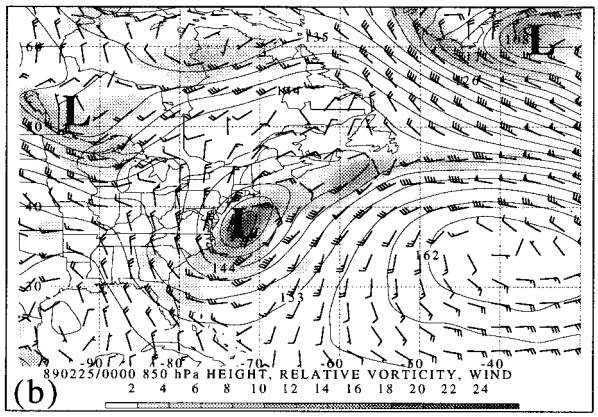

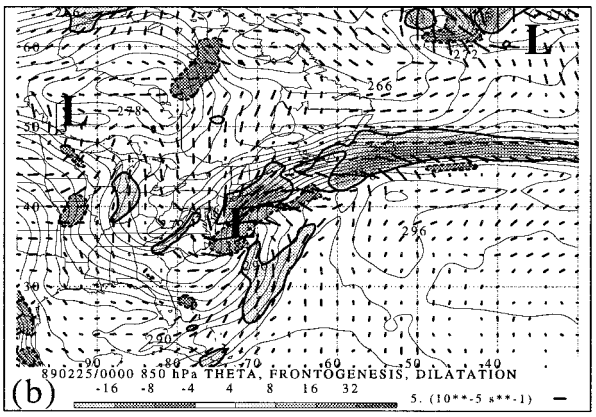

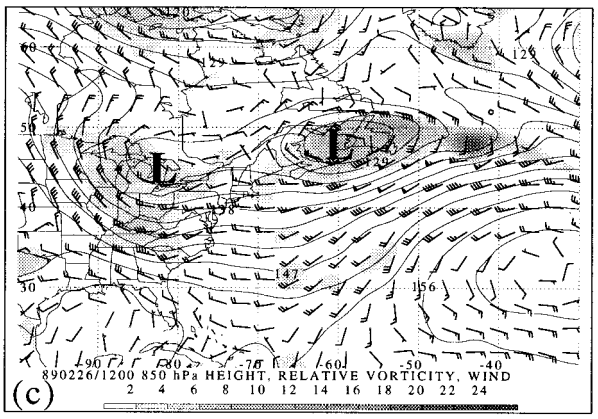

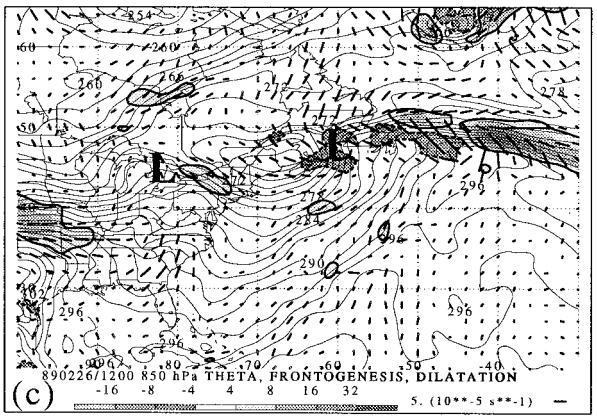

FIG. 6. As in Fig. 2 except for IOP8: (a) 1200 UTC 23 February 1989; (b) 0000 UTC 25 February 1989; (c) 1200 UTC 26 February 1989.

FIG. 7. As in Fig. 3 except for IOP8: (a) 1200 UTC 23 February 1989; (b) 0000 UTC 25 February 1989; (c) 1200 UTC 26 February 1989.

clusion, we feel that IOP8 provides a representative example of a Shapiro–Keyser cyclone.

The 300-hPa flow associated with IOP8 was characterized by large-scale confluence (Figs. 8a–c), which may be contrasted with the large-scale diffluence characterizing ATL1 (Figs. 4a–c). The 850-hPa low center over South Carolina that would eventually become IOP8 was located beneath the left entrance region of an extremely strong (95 m s^{-1}), anticyclonically curved, 300-hPa jet maximum along the east coast of North America at 23/12 (Fig. 8a). By 25/00, the maximum wind speed increased, in association with the merger of the jet maximum with the poleward branch of the jet stream located to the southwest of Greenland (Fig. 8b). At 26/12, the 850-hPa cyclone northeast of Nova Scotia moved northeastward as the principal 300-hPa jet maximum moved eastward (Fig. 8c).

The scale-partitioned flow shows that the 850-hPa high-pass cyclone is of similar scale and intensity to that of ATL1 (about 400 km in radius and −8 to −11

dam, respectively), but becomes more zonally elongated in the low-pass confluence (cf. Figs. 5a,c and 9a,c). In addition, the low-pass flow fields at 850 and 300 hPa indicate that tropospheric-deep confluence and stronger wind speeds are found downstream of the cyclone at both 25/00 and 26/12 (Figs. 9a–d).

c. Discussion: Norwegian versus Shapiro–Keyser cyclones

In the present discussion, we wish to consider in more detail how the large-scale flow in which the cyclone is embedded affects the resulting cyclone/frontal structure and evolution. Based upon ATL1, two other North Atlantic cyclones on 4–6 January 1989 and 7–9 February 1988 described by Schultz (1996, sections 4.2 and 4.6, respectively), and a case over the central United States on 14–16 December 1987 (Schultz and Mass 1993), the Norwegian occlusion appears to occur when large-scale diffluence is found downstream of the cyclone. The diffluence acts in two ways to produce a Norwegian occlusion. First, the 850-hPa dilatation axes over the cyclone are generally meridionally oriented due to the diffluence, favoring meridionally elongated vorticity features and fronts (Figs. 2c and 3c). As illustrated schematically in Fig. 10a [based mainly on ATL1 (Fig. 3c)], the axes of dilatation along most of the length of the cold, warm, and occluded fronts lie nearly parallel to the isentropes, resulting in frontogenesis along either side of the warm sector. This relationship favors an intense meridionally oriented cold front with a well-defined poleward extension (i.e., no frontal fracture). If the deformation over the cyclone is large enough and the axes of dilatation are oriented meridionally, then the warm front may rotate anticyclonically [as described in Bishop (1996)]. The anticyclonically rotating warm front, along with the cyclonically rotating cold front, result in the narrowing of the warm sector over time, forming a Norwegian occlusion. Second, as the cyclone begins to move more poleward and less eastward, the eastward-moving cold air equatorward of the low center (K in Fig. 10a) is more likely to surround the low center, forming a Norwegian occlusion (i.e., the cold air is advancing eastward in a storm-relative framework).

In contrast, IOP8 evolved within large-scale confluence, forming features resembling the Shapiro–Keyser cyclone model. As illustrated schematically in Fig. 10b [based mainly on IOP8 (Fig. 7b)], the large-scale confluence generally acts to orient the axes of dilatation zonally over the cyclone, resulting in a strong, zonally oriented warm front. The T-bone frontal structure of a Shapiro–Keyser cyclone implies that the orientation of the isentropes changes abruptly from primarily meridional along the poleward end of the cold front to primarily zonal along the warm front. At the region of the frontal fracture, an unfavorable relationship for frontogenesis exists between the axes of dilatation and the isentropes; the axes of dilatation and isentropes generally lie perpendicular to each other such that the deformation acts to spread the isentropes apart. A similar frontolytical configuration occurs at the southwestern end of the bent-back front. Because of the strong winds often observed along the bent-back front and the eastward motion of the cyclone center, it is unlikely that the bulk of the cold air west of the bent-back front (K in Fig. 10b) can wrap around south of the low center as it does in the Norwegian cyclone model (cf. Figs. 10a,b).

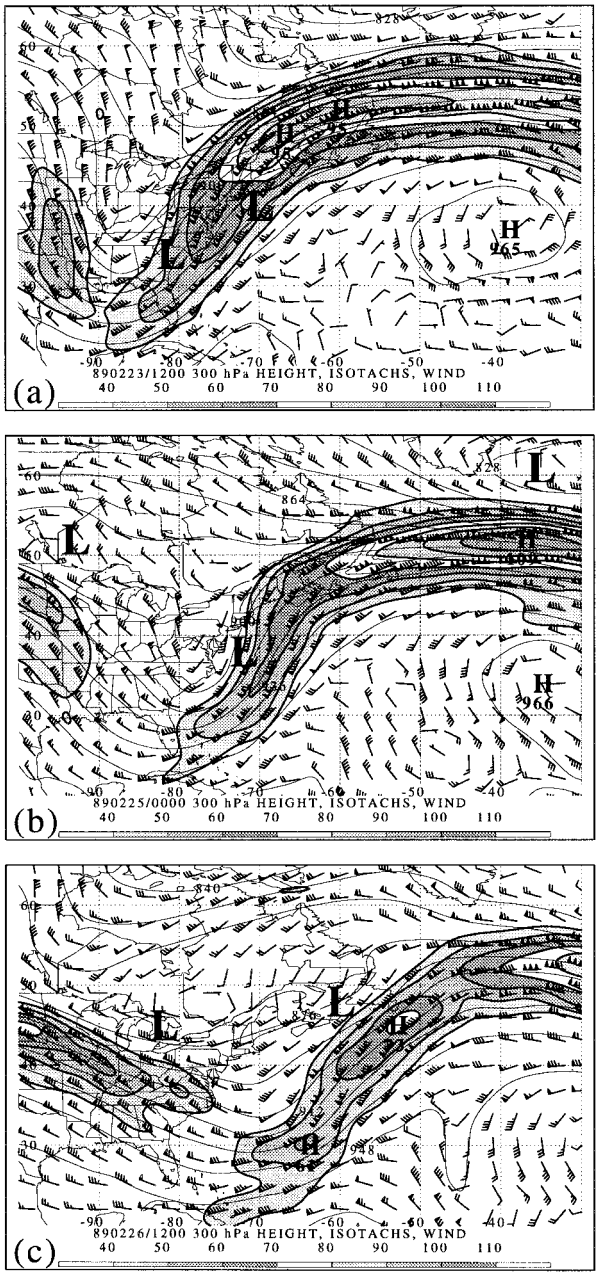

FIG. 8. As in Fig. 4 except for IOP8: (a) 1200 UTC 23 February 1989; (b) 0000 UTC 25 February 1989; (c) 1200 UTC 26 February 1989.

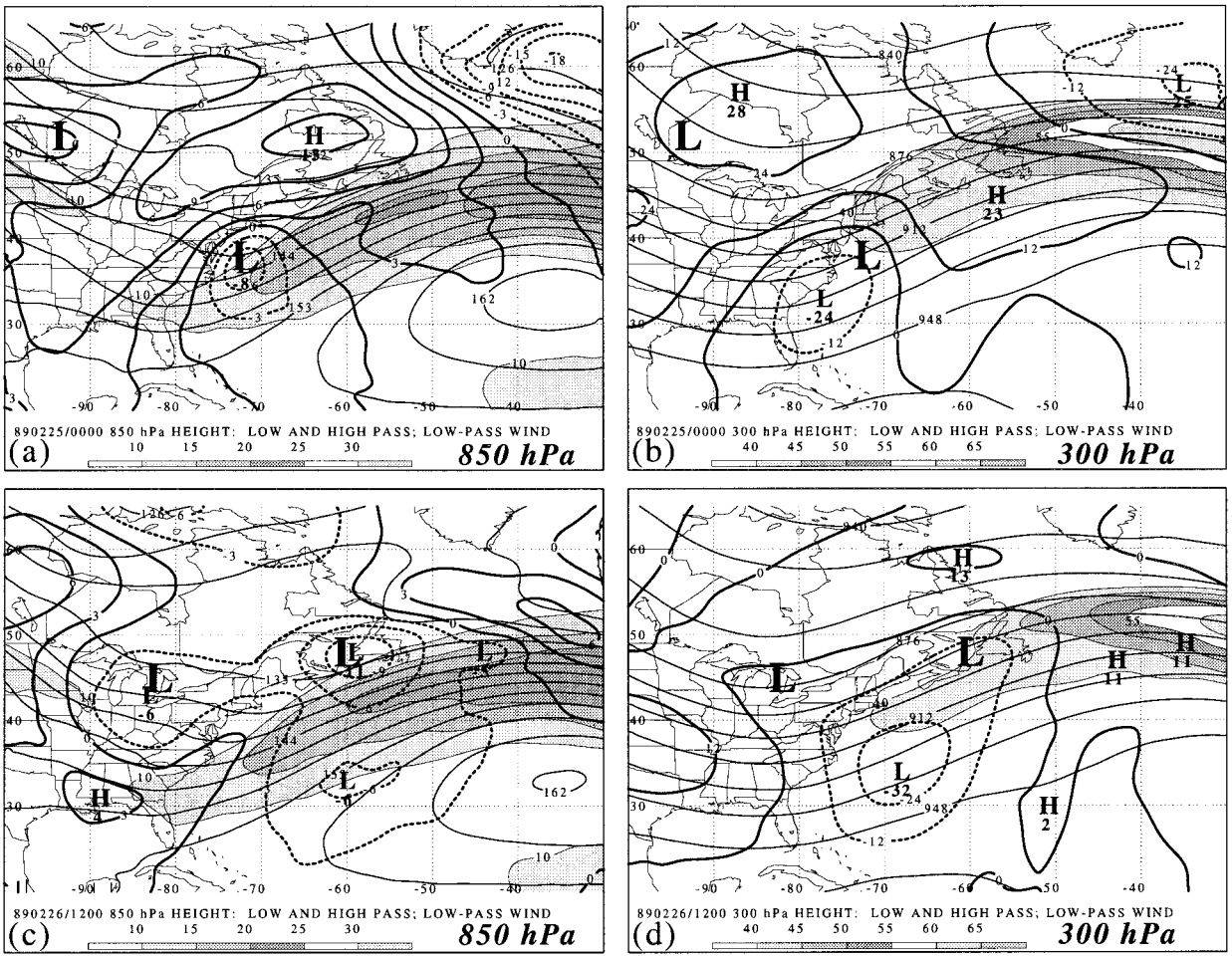

FIG. 9. As in Fig. 5 except for IOP8: 0000 UTC 25 February 1989 in (a) and (b); 1200 UTC 26 February 1989 in (c) and (d).

That the cold and warm fronts either are merging to form a thermal ridge as in the Norwegian cyclone, or are oriented nearly perpendicular to each other as in the Shapiro–Keyser cyclone, implies that these structures generally should not be found simultaneously in the same cyclone. Nevertheless, this difference in the configuration of the cold and warm fronts does not preclude the possibility that individual cyclones may transition from one conceptual model to the other. This hypothesized transition is supported by baroclinic channel-model simulations that tend to resemble the Shapiro–Keyser model early in their life cycle when the large-scale flow is relatively zonal and the Norwegian model later when the large-scale flow becomes more highly amplified (S. Mudrick 1991, personal communication; Thompson 1995). Furthermore, the frequent development of strongly diffluent downstream ridges during the course of cyclogenesis (e.g., Vederman 1954; Palmén and Newton 1969, 335; Carlson 1991, 232; Orlanski and Sheldon 1995) suggests that observed cyclones would tend to evolve more Norwegian-like characteristics later in their life cycles [e.g., ERICA IOP 4 as discussed by Shapiro and Donall Grell (1994)].

4. Idealized vortex model

To test whether the structural and evolutionary differences in the two observed cyclones described in the previous section can be attributed to the large-scale flow in which each cyclone was embedded (diffluence in ATL1 versus confluence in IOP8), a time-dependent nondivergent barotropic model that treats potential temperature as a conserved passive tracer (except for weak numerical diffusion) is considered in this section. To abstract these observed cases, an idealized vortical flow of the same form as in Doswell (1984) is placed in various background flows that are simplifications of those from ATL1 and IOP8. The goal in applying this idealized model is to illustrate that deformation in nondivergent flow concentrates isentropes in certain regions relative to the vortex, producing fronts of a preferred shape and orientation that depend on the background

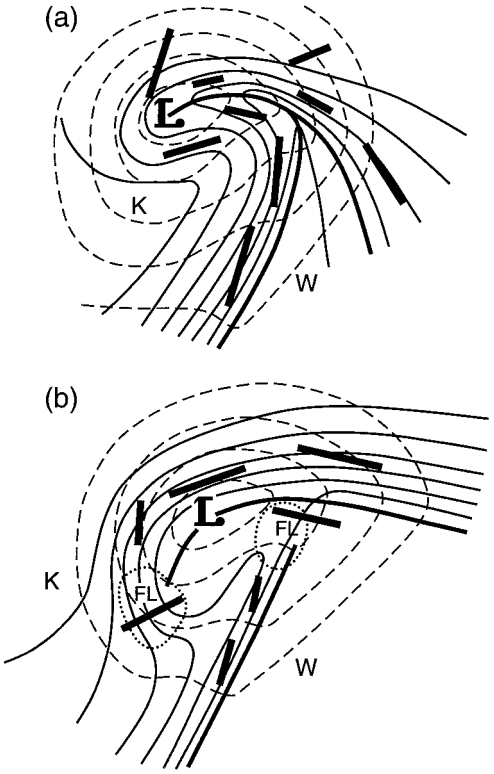

FIG. 10. Schematic comparison of the lower-tropospheric (e.g., 850-hPa) structure of (a) the Norwegian occlusion and (b) the Shapiro–Keyser frontal fracture. Dashed lines denote geopotential height; thin solid lines denote potential temperature; thick solid lines represent fronts; and thick line segments represent axes of dilatation of total horizontal wind with segment length proportional to the resultant deformation. Areas surrounded by dotted lines labeled FL in (b) represent regions of frontolysis, and K and W in (a) and (b) denote cold and warm regions of the cyclones, respectively. The characteristic scale of the cyclones based on the distance from the geopotential height minimum, denoted by L, to the outermost geopotential height contour is 1000 km.

flow. Therefore, kinematic processes may explain much of the observed structure and evolution of synoptic-scale fronts in midlatitude oceanic cyclones.

a. Methodology

In order to extend the present analysis beyond the analytically tractable problem of steady-state flows (e.g., Doswell 1984, 1985; Davies-Jones 1985), a time-dependent nondivergent barotropic model on an f plane is employed to describe the evolution of vortices in various idealized large-scale flows. The model is that of Smith et al. (1990) with the following four modifications. First, a prognostic equation for a passive tracer representing potential temperature is included; the tracer distribution is integrated forward in time at each model time step using a second-order Adams–Bashforth scheme. Second, the model domain is generalized from a zonally periodic channel to an open (no walls), nonperiodic domain. The horizontal boundary conditions for the computational domain are as follows. For the case with zero background flow, a Dirichlet condition of zero relative vorticity on the boundaries is employed. For the cases with nonzero background flow, a Neumann condition of zero relative vorticity gradient normal to the boundaries is employed. The streamfunction is diagnosed from the relative vorticity on the interior of the domain, given values of the streamfunction on the boundaries. For all cases, the streamfunction on the boundaries is set to its initial value throughout the simulation, a simplification justified by the temporal invariance of the background flow and by the observation that the vortex remains well away from the boundaries. Third, the geopotential height h is diagnosed from the streamfunction ψ using the nonlinear balance equation:

$$g\nabla^2 h = f_0\nabla^2\psi + \frac{1}{2}(\zeta^2 - E^2), \tag{5}$$

where $g = 9.81$ m s^{-2}, $f_0 = 9.37 \times 10^{-5}$ s^{-1}, applicable at 40°N, and $\zeta = \partial v/\partial x - \partial u/\partial y$. For the case with zero background flow, a Dirichlet condition of $h = f_0\psi/g$ is adopted at the horizontal boundaries. The boundary condition for the cases with nonzero background flow is introduced in section 4c. Fourth, the data are output to GEMPAK for display and diagnosis.

The barotropic model is implemented with the following specifications. The model time step is 60 s. The horizontal grid spacing is 29.6 km on a domain of 151 $\times$ 151 grid points (4440 km $\times$ 4440 km) for $-x_{\max} < x < x_{\max}$ and $-y_{\max} < y < y_{\max}$, where $x_{\max}$ and $y_{\max}$ are the half-length and half-width of the computational domain, respectively (2220 km).

The simplifications arising from the present methodology limit the applicability of the model simulations to observed fronts and cyclones for the following reasons. First, the Norwegian occlusion process cannot occur in the same manner as in the real atmosphere. Since the barotropic model is nondivergent, the surface area between isentropes in the warm sector is conserved, so that the warm sector can only be deformed into a thin ridge; the width of the thermal ridge cannot be decreased by convergence as in observations of occluding cyclones (e.g., Schultz and Mass 1993, their Fig. 15). Second, in these simulations, a fully developed steady-state vortex begins operating on a diffuse frontal zone. This initial state contrasts with many observations of growing type-B cyclones (e.g., Petterssen et al. 1962; Petterssen and Smebye 1971), including ATL1 and IOP8 (Figs. 2–3 and 6–7, respectively), where the intensity of the cyclones and the strength of the low-level frontal zones increase simultaneously. Finally, the feedback between the potential temperature and the horizontal wind fields during frontogenesis (e.g., Hoskins and Bretherton 1972) is not included since divergent circulations are absent. Nevertheless, the extent to which these idealized simulations realistically reproduce various aspects of synoptic-scale cyclone/frontal structure and evolution is

encouraging, given the considerable simplifications inherent to the methodology adopted in this section.

b. Circular Doswell vortex in zero background flow: Control case (CONT)

This idealized modeling work is based on that of Doswell (1984), who examined the structure and evolution of an initially straight frontal zone acted upon by a nondivergent, steady-state vortex. Using an analytical approach, Doswell (1984) specified idealized distributions of horizontal velocity and potential temperature that, upon integration in time, yielded the evolution of the isentropes and frontogenesis. Continued integration of his model was limited by the complexity of the resulting analytical solutions. Davies-Jones (1985) later extended Doswell's vortex model by developing a general class of closed-form solutions based on the restrictions that the vortex be circularly symmetric and that the initial potential temperature field be one-dimensional. Davies-Jones confirmed Doswell's basic results despite the truncation errors from the large time step in Doswell's integration scheme. In his reply, Doswell (1985) presented solutions using Davies-Jones' analytical results, thereby extending the vortex evolution further into the nonlinear regime. Finally, analytical solutions to the spatial pattern and evolution of the frontogenesis vector **F** [a generalization of (1) that includes the rate of change of the direction of $\nabla\theta$] and its divergence for the Doswell vortex were presented by Keyser et al. (1988).

Doswell (1984) defined the nondimensional tangential velocity $\tilde{V}_T$ of his vortex as

$$\tilde{V}_T(\tilde{r}) = \tanh\tilde{r}\,\cosh^{-2}\tilde{r}, \tag{6}$$

where $\tilde{r}$ is the nondimensional radius from the center of the vortex. Equation (6) gives a radial distribution of the tangential velocity, which is zero at $\tilde{r} = 0$ and $\tilde{r} = \infty$ and has a maximum of approximately 0.3849 at $\tilde{r} \approx 0.6585$. For this paper, we choose a dimensional form (tildes dropped)

$$V_T(r) = \left(\frac{V_{\max}}{0.3849}\right)\tanh\left(\frac{r}{r_v}\right)\cosh^{-2}\left(\frac{r}{r_v}\right), \tag{7}$$

where $V_{\max}$ is the maximum tangential wind speed, and r_v is the scaling radius (radius of maximum wind divided by 0.6585). In Cartesian coordinates, the horizontal wind components $\mathbf{V} = (u, v)$ are

$$u = -V_T(r)\sin\phi, \tag{8}$$

$$v = V_T(r)\cos\phi, \tag{9}$$

where ϕ is the azimuth angle rotated counterclockwise from the positive x axis. This vortex can be thought of as a smoothly varying analog to the widely used Rankine combined vortex (Doswell 1984), which has a discontinuity in tangential-velocity gradient at the outer edge of the vortex. The criterion for isolation [i.e., the integrated relative vorticity from $r = 0$ to $r = \infty$ is equal to zero (Hopfinger and van Heijst 1993, 248)] is satisfied for this vortex.

The specific vortex used in the simulations in this section, hereafter referred to as the control case (CONT) when in the absence of background flow, is illustrated in Fig. 11. In this case, $V_{\max} = 10$ m s^{-1} and $r_v = 500$ km, values typical of the 850-hPa high-pass wind speed (not shown) and height (Figs. 5a,c and 9a,c) fields for ATL1 and IOP8. These values yield radii of maximum tangential wind speed and deformation at 329 km ($0.6585r_v$) and 435 km ($0.8695r_v$), respectively (Fig. 11a). The axes of dilatation for CONT are rotated 45° cyclonically to the streamfunction everywhere in the vortex, and the maximum deformation is 3.38×10^{-5} s^{-1} (Fig. 11a). The relative vorticity achieves a maximum of 10.3×10^{-5} s^{-1} at the center of the vortex (Fig. 11b), decreases to zero at 505 km ($1.0096r_v$), and is surrounded by a ring of anticyclonic vorticity with a minimum of -0.81×10^{-5} s^{-1} at 718 km ($1.4366r_v$). At the center of the vortex the minimum height is equal to -7.7 dam (Fig. 11b), comparable to the high-pass 850-hPa heights at the low centers during the early stages of ATL1 and IOP8 (Figs. 5a and 9a), respectively.

Doswell (1984) considered the nondimensional passive-tracer field of potential temperature $\tilde{\theta}$ to be of the form

$$\tilde{\theta}(\tilde{y}) = -\tanh\tilde{y}, \tag{10}$$

yielding a zonally oriented frontal zone with the maximum gradient at the center of the zone, decreasing to zero gradient at large $|\tilde{y}|$. Dimensionalizing (10) results in

$$\theta(y) = \theta_0 - \frac{\Delta\theta}{2}\frac{\tanh(y/y_r)}{\tanh(y_{\max}/y_r)}, \tag{11}$$

where θ_0 is a reference value of potential temperature (290 K), $\Delta\theta$ is the difference in potential temperature across the frontal zone (20 K), y_r is the scaling of the width of the potential temperature gradient (500 km, the same scaling as for the tangential wind r_v), and $y_{\max}$ is as defined in section 4a. The denominator, $\tanh(y_{\max}/y_r)$, serves to confine the entire range of $\Delta\theta$ within the computational domain.

Although only one radial profile of the tangential wind and one distribution of potential temperature [those of Doswell (1984)] are considered in this paper, Schultz (1996, section 5.7) presented the frontal evolution for other vortex and frontal-zone profiles. For example, vortices were considered with tangential-velocity profiles given by the beta probability distribution with $a = 2$ and $b = 4$ (Ross 1984, 174–175), Chan and Williams (1987), and Smith et al. (1990), respectively. These three vortices have the property that $V_T(r)$ is zero at the center of the vortex and at some (finite or infinite) radial distance and is maximum in between. Except for details in the frontal structure close to the center of the vortex, the evolutions for the three vortices were qualitatively similar to that

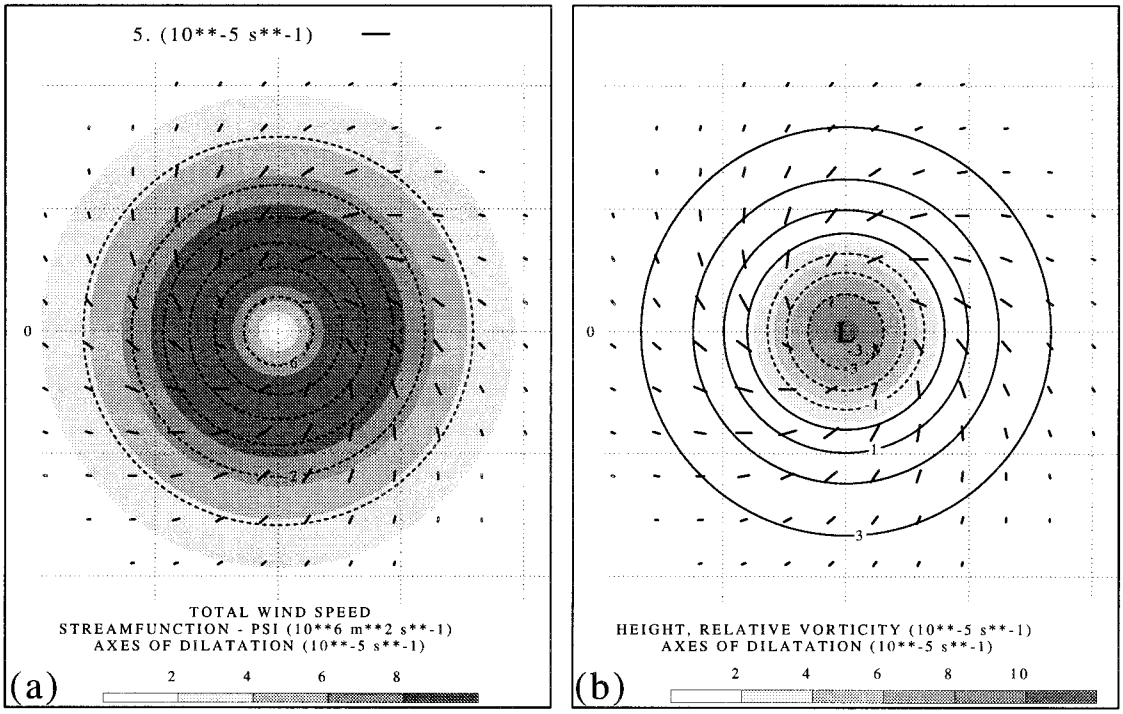

FIG. 11. Kinematics of the circular Doswell vortex in zero background flow (CONT); *x*- and *y*-coordinate lines dotted every 500 km, $y = 0$ labeled "0," and axes of dilatation of horizontal wind [10^{-5} s^{-1}, scaled according to legend in (a); separation between displayed axes of dilatation is 148 km (every fifth grid point)]. Only a portion of the computational domain is shown: (a) streamfunction (dashed lines every 1×10^6 m^2 s^{-1}) and horizontal wind speed (m s^{-1}, shaded according to scale at bottom of figure); (b) relative vorticity of horizontal wind (10^{-5} s^{-1}, shaded according to scale at bottom of figure) and geopotential height [positive and zero (negative) values solid (dashed) every 1 dam]; L represents location of minimum geopotential height.

for the Doswell vortex. Using a frontal zone specified by a constant potential temperature gradient and varying y_r in (11) to change the width of the frontal zone also yielded results similar to those for the Doswell vortex. In summary, the resulting frontal structures and evolutions appear to be relatively insensitive to the detailed specification of the vortex or frontal zone for realistic specifications of these features.

Figure 12 illustrates the evolution of CONT. Since the horizontal divergence is zero in the barotropic model, (2) reduces to (3) so that the total frontogenesis is due to horizontal deformation only ($F = F_E$). At 0 h (Figs. 12a,d), a four-cell frontogenesis pattern illustrates that frontogenesis (frontolysis) occurs northeast and southwest (northwest and southeast) of the vortex center along the frontal zone. By 12 h into the simulation (Fig. 12b), the cold and warm air are advected around the vortex, forming the characteristic S-shape to the isentropes noted by Doswell (1984). The values of maximum frontogenesis double in magnitude, and the pattern of frontogenesis becomes focused along two bands northeast and southwest of the vortex center (hereafter called the warm front and cold front, respectively), whereas the regions of frontolysis decrease in size and intensity (Fig. 12e). Since the vortex tends to rotate the isentropes into a configuration that is nearly parallel to the axes of dilatation [a point noted by Doswell (1984) and Davies-Jones (1985)], the area occupied by frontogenesis compared to frontolysis increases with time. At the center of the vortex, where the resultant deformation is equal to zero (Fig. 11a), the frontogenesis is exactly zero (Figs. 12d–f), and thus the potential temperature gradient remains constant (Figs. 12a–c; Doswell 1984).

By 24 h, the frontal zones tighten into sharp fronts that spiral around the vortex nearly parallel to the dilatation axes as the regions of frontolysis continue to shrink in size and magnitude (Figs. 12c,f). At this stage, the structure of the frontal zones (Fig. 12c) is reminiscent of the frontal T-bone and frontal fracture presented in IOP8 (Fig. 7b) and in the schematic diagram of a Shapiro–Keyser cyclone (Fig. 10b) in that the poleward portion of the cold front is nearly perpendicular to the warm front and is separated from the warm front by a region of weak frontolysis. The band of frontogenesis associated with the warm front extends into the equatorward flow west of the vortex (Fig. 12f), resembling the bent-back front in IOP8 (Fig. 7b) and in the schematic (Fig. 10b).

Further integration of CONT (not shown) results in the cold and warm fronts continuing to lengthen and spiral around the vortex. Consequently, the width of the

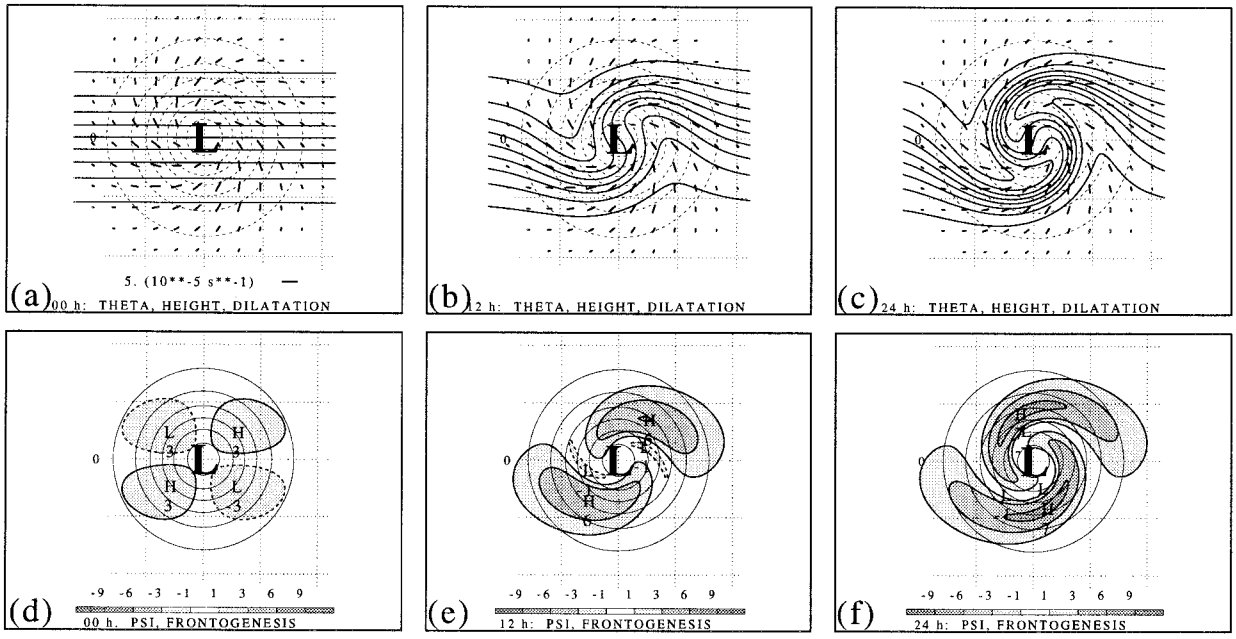

FIG. 12. Evolution of the circular Doswell vortex in zero background flow (CONT) at 0 h [(a) and (d)], 12 h [(b) and (e)], and 24 h [(c) and (f)]; *x*- and *y*-coordinate lines dotted every 500 km, $y = 0$ labeled "0," and large L's represent locations of minimum streamfunction. Only a portion of the computational domain is shown. Top: potential temperature (solid lines every 2 K), streamfunction (dashed lines every 1×10^6 m^2 s^{-1}), and axes of dilatation of horizontal wind [10^{-5} s^{-1}, scaled according to legend in (a); separation between displayed axes of dilatation is 148 km (every fifth grid point)]. Bottom: geopotential height (solid lines every 1 dam) and frontogenesis due to horizontal wind [10^{-1} K (100 km)$^{-1}$ (3 h)$^{-1}$, contoured and shaded according to scale at bottom of figure; positive (negative) values solid (dashed)]; small H's and L's represent maxima and minima of frontogenesis, respectively.

thermal ridge continues to decrease, resembling the occlusion process in the Norwegian cyclone model. This narrowing of the thermal ridge would continue until limited by the horizontal grid resolution.

c. Circular Doswell vortices in pure stretching deformation

To test whether the differences between the observed frontal structures and evolutions of ATL1 and IOP8 (Figs. 5a,c and 9a,c) may be attributed to the diffluent or confluent background flow, respectively, the circular Doswell vortex is placed in simplifications of those large-scale flows. Bergeron (1928) recognized the frontogenetic properties of pure stretching deformation and many have used it since [e.g., Keyser et al. (1988, 767) provide a list of those studies]. The streamfunction for pure stretching deformation can be written

$$\psi = -\alpha(x - x_{\text{ref}})y, \tag{12}$$

where α is the deformation parameter and x_{ref} is a constant indicating the location of the y asymptote of the flow. The resulting horizontal wind components are

$$u = \alpha(x - x_{\text{ref}}), \tag{13}$$

$$v = -\alpha y. \tag{14}$$

In this case, both the stretching and resultant deformation of the background flow equal 2α, whereas the shearing deformation, relative vorticity, and horizontal divergence of the background flow are equal to zero. To solve (5) for the geopotential height, a Dirichlet condition on the horizontal boundaries is determined from an exact solution to (5), a form of which can be found in Keyser and Pecnick [1985, (2.8)]:

$$h = -\frac{f_0}{g}\alpha(x - x_{\text{ref}})y - \frac{1}{2}\frac{\alpha^2}{g}[(x - x_{\text{ref}})^2 + y^2]. \tag{15}$$

In order to isolate the vortex from the background flow, the geopotential height field of the vortex is determined by subtracting the background geopotential height field from the total geopotential height field, where these latter fields are diagnosed from (5) in conjunction with (15) on the horizontal boundaries. For the simulation involving diffluent background flow, $\alpha = -4.5 \times 10^{-6}$ s^{-1} [-10 m s^{-1} (2220 km)$^{-1}$] and $x_{\text{ref}} = x_{\max}$, whereas for confluent background flow, $\alpha = 4.5 \times 10^{-6}$ s^{-1} and $x_{\text{ref}} = -x_{\max}$.

1) CIRCULAR DOSWELL VORTEX IN DIFFLUENCE (DIFF)

The evolution of the control case plus diffluence (hereafter DIFF) is displayed in Fig. 13. Since the back-

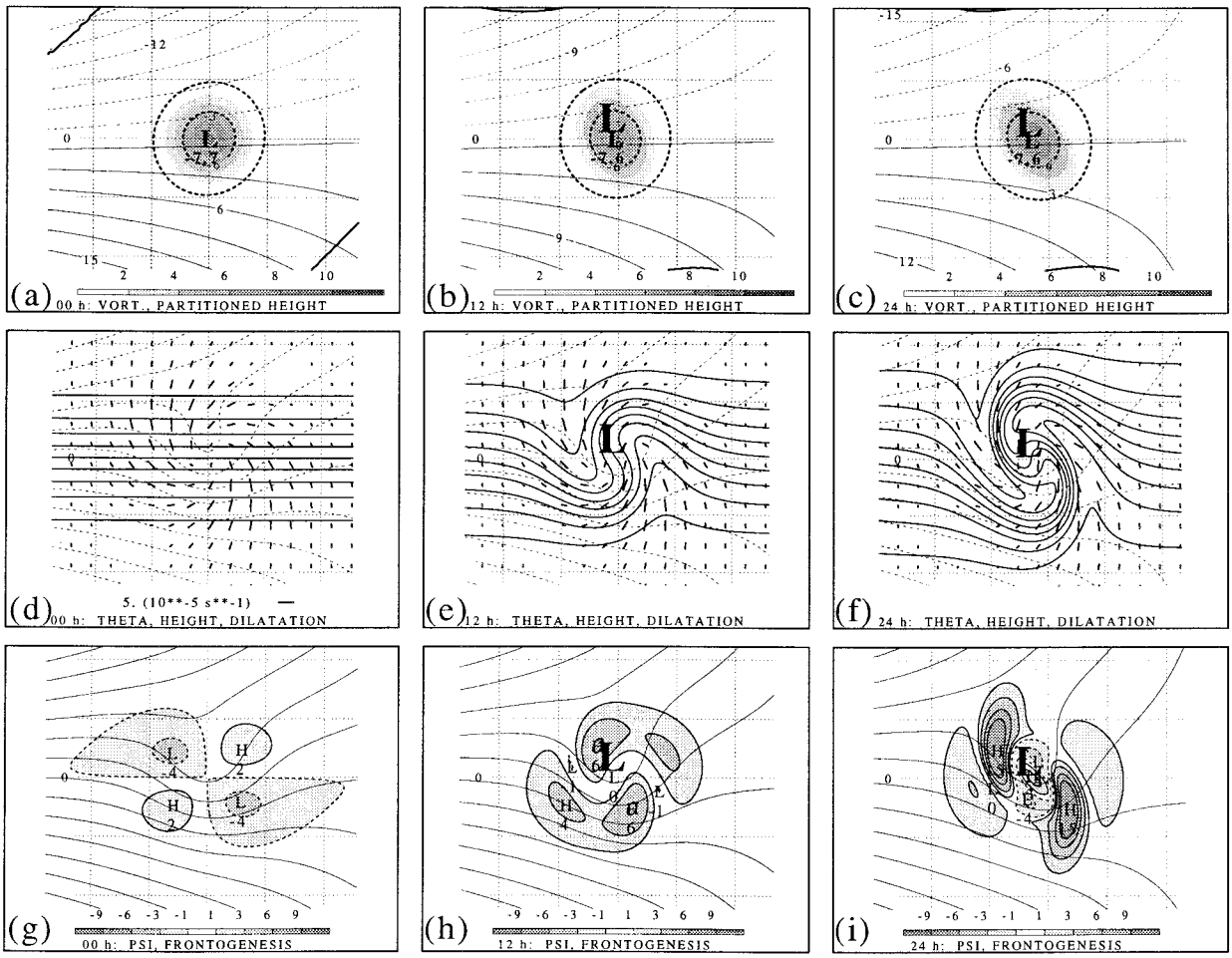

FIG. 13. Evolution of circular Doswell vortex in diffluent background flow (DIFF) at 0 h [(a), (d), and (g)], 12 h [(b), (e), and (h)], and 24 h [(c), (f), and (i)]; x- and y-coordinate lines dotted every 500 km, $y = 0$ labeled "0," and large L's represent locations of minimum total streamfunction. Only a portion of the computational domain is shown. Top: geopotential height of the background flow [thin lines every 3 dam; positive and zero (negative) values solid (dashed)], geopotential height of the vortex [thick lines every 3 dam; positive and zero (negative) values solid (dashed); small L's represent minima of geopotential height of the vortex], and relative vorticity of total horizontal wind (10^{-5} s^{-1}, shaded according to scale at bottom of figure). Middle: potential temperature (solid lines every 2 K), total geopotential height (dashed lines every 3 dam), and axes of dilatation of total horizontal wind [10^{-5} s^{-1}, scale in (d); separation between displayed axes of dilatation is 148 km (every fifth grid point)]. Bottom: total streamfunction (solid lines every 3×10^6 m^2 s^{-1}) and frontogenesis due to total horizontal wind [10^{-1} K (100 km)$^{-1}$ (3 h)$^{-1}$, contoured and shaded according to scale at bottom of figure; positive (negative) values solid (dashed)]; small H's and L's represent maxima and minima of frontogenesis, respectively.

ground diffluence has no vorticity, the total vorticity for DIFF is due solely to the vortex (Fig. 13a).[4] In time, the background diffluence elongates the vorticity field (Fig. 13b), so that by 24 h the vorticity and height associated with the vortex in DIFF are elongated northwest–southeast (Figs. 13c). Once the vortex is no longer circularly symmetric, it rotates cyclonically and changes shape as it evolves, eventually forming filaments (tails of cyclonic vorticity or troughs in the streamfunction that extend outward from the edge of the vortex in the direction of the major axis) (e.g., Melander et al. 1987;

[4] The streamfunction and vorticity fields for the Doswell vortex in background diffluence or confluence are circularly symmetric at the initial time, but the height field is not circularly symmetric (Figs. 13a and 14a). Note, however, that the height field for the Doswell vortex in the absence of background flow is circularly symmetric (Fig. 11b). The asymmetry in the height field in the cases with background flow arises from the second term on the right-hand side [$\frac{1}{2}(\zeta^2 - E^2)$] of the nonlinear balance equation (5) used to solve for the height field (section 4a). Since the vorticity is equal in the cases with the Doswell vortex in background stretching deformation and in zero background flow, the interaction of the background deformation with the vortex deformation is responsible for producing the asymmetry. This term in the nonlinear balance equation also is responsible for the negative-definite contribution to the height field arising from the second term on the right-hand side of (15), which explains the lack of symmetry of the background height fields with respect to the centerline of the domain ($y = 0$) (Figs. 13a and 14a).

Guinn and Schubert 1993). The dilatation axes in DIFF approach those of the background flow (meridionally oriented) away from the influence of the deformation associated with the vortex (Fig. 13d). Additionally, the meridionally oriented dilatation axes associated with the background diffluence and the meridionally oriented dilatation axes associated with the vortex northwest and southeast of the vortex center[5] (Fig. 11b) combine to maximize the deformation and to produce frontolysis in these areas (Figs. 13d,g). In contrast, the meridionally oriented dilatation axes associated with the background diffluence and the zonally oriented dilatation axes associated with the vortex northeast and southwest of the vortex center (Fig. 11b) offset each other, decreasing the total deformation[6] and producing weak frontogenesis in these areas (Figs. 13d,g).

As the simulation progresses, the isentropes are advected into a frontogenetical configuration with respect to the axes of dilatation north-northwest and south-southeast of the vortex center (cf. Figs. 13d,e), yielding the rapid formation of meridionally elongated regions of frontogenesis, separated by a small region of near-zero frontogenesis near the vortex center (Fig. 13h), similar to ATL1 at 9/12 (Fig. 3b). Secondary maxima of frontogenesis are located east-northeast and west-southwest of the vortex center (Figs. 13e,h). By 24 h, the fronts in DIFF sharpen dramatically and continue to rotate around the cyclone (Figs. 13f,i). As was the case for ATL1 at 10/00 (Fig. 3c), the fronts in DIFF are elongated meridionally, and the warm and cold sectors narrow in width (Figs. 13f,i). Also, the strong deformation southeast of the vortex behind the cold front (Fig. 13f) is apparent in ATL1 (Fig. 3b).

A significant difference between observed cyclones in general and the idealized vortex model simulations (illustrated for the present discussion by ATL1 and DIFF) is that the maximum potential temperature gradient and frontogenesis along the cold and warm fronts may differ by a factor of 2 or more in observed cyclones (e.g., Fig. 3a), but remain equal along the cold and warm fronts throughout the idealized model simulation (Figs. 13d–f,g–i). Several hypotheses as to why this asymmetry exists in the real atmosphere are now proposed. First, Schultz (1996, section 5.7.4) showed that including the latitudinal variation of the planetary vorticity (the beta effect) in the control case leads to asymmetries in the streamfunction that enhance the deformation and frontogenesis along the warm front relative to the cold front, resulting in a maximum potential temperature gradient along the warm front that is 17% greater than the maximum potential temperature gradient along the cold front at 24 h. This effect, however, appears to be too small to explain the magnitude of the asymmetries in observed cyclones. Second, variability (both spatial and temporal) of the background flow in the vicinity of an observed cyclone can be important to the asymmetry between the cold and warm fronts, but this effect is not addressed in the idealized simulations because of the use of the simplified velocity specification [(13) and (14)] in which α is constant. A related point is that the deformation associated with the high-pass wind fields in the vicinity of observed cold and warm fronts is not likely to be equal. Third, regardless of background flow, most observed cold fronts eventually become meridionally elongated, whereas most observed warm fronts eventually become zonally elongated. For example, since background diffluence generally is characterized by meridionally oriented axes of dilatation (i.e., in the exit region of a zonally oriented jet stream), meridionally oriented cold fronts and the suppression of zonally oriented warm fronts would be favored. Similarly, since background confluence generally is characterized by zonally oriented axes of dilatation (i.e., in the entrance region of a zonally oriented jet stream), zonally oriented warm fronts and the suppression of meridionally elongated cold fronts would be favored. Finally, as noted in section 4a, the barotropic model used in this study is nondivergent. Calculations for observed cases (including ATL1 and IOP8) suggest that divergence and F_D (4) may be stronger along warm fronts than cold fronts (not shown).

Another difference between ATL1 and DIFF is that the warm front in ATL1 remains on the northeast side of the cyclone, whereas the warm front in DIFF rotates around to the northwest side of the vortex (cf. Figs. 3c and 13f). A plausible explanation for this difference is the absence of divergent flow and advection of potential temperature by this flow component in the barotropic model. For example, north of observed cyclones, the low-level divergent flow tends to be from the west or northwest,[7] partially counteracting the advection of the warm-sector air by the nondivergent cyclonic flow. Therefore, the absence of divergence in the barotropic model may lead to the warm air advancing too far cyclonically around the vortex. Note that the presence of divergent flow behind observed cold fronts (usually westerly) should accelerate the formation of a Norwegian occlusion, consistent with the comment made in section 3c that the eastward advance of the cold air in a storm-relative framework equatorward of the low center is conducive to the formation of a Norwegian oc-

[5] The vortex center is defined as the location of maximum vorticity, which also corresponds to the minimum geopotential height of the vortex.

[6] It may be shown that the addition of two flow fields characterized by equal resultant deformation but orthogonal dilatation axes at a given point yields zero resultant deformation at that point.

[7] For illustrations of the low-level divergent flow in observed cyclones, see, for example, Loughe et al. (1995, Fig. 2a) and Schultz et al. (1997, Fig. 7c), and in idealized channel model simulations of baroclinic development; see, for example, Keyser et al. (1989, Figs. 7b and 11b).

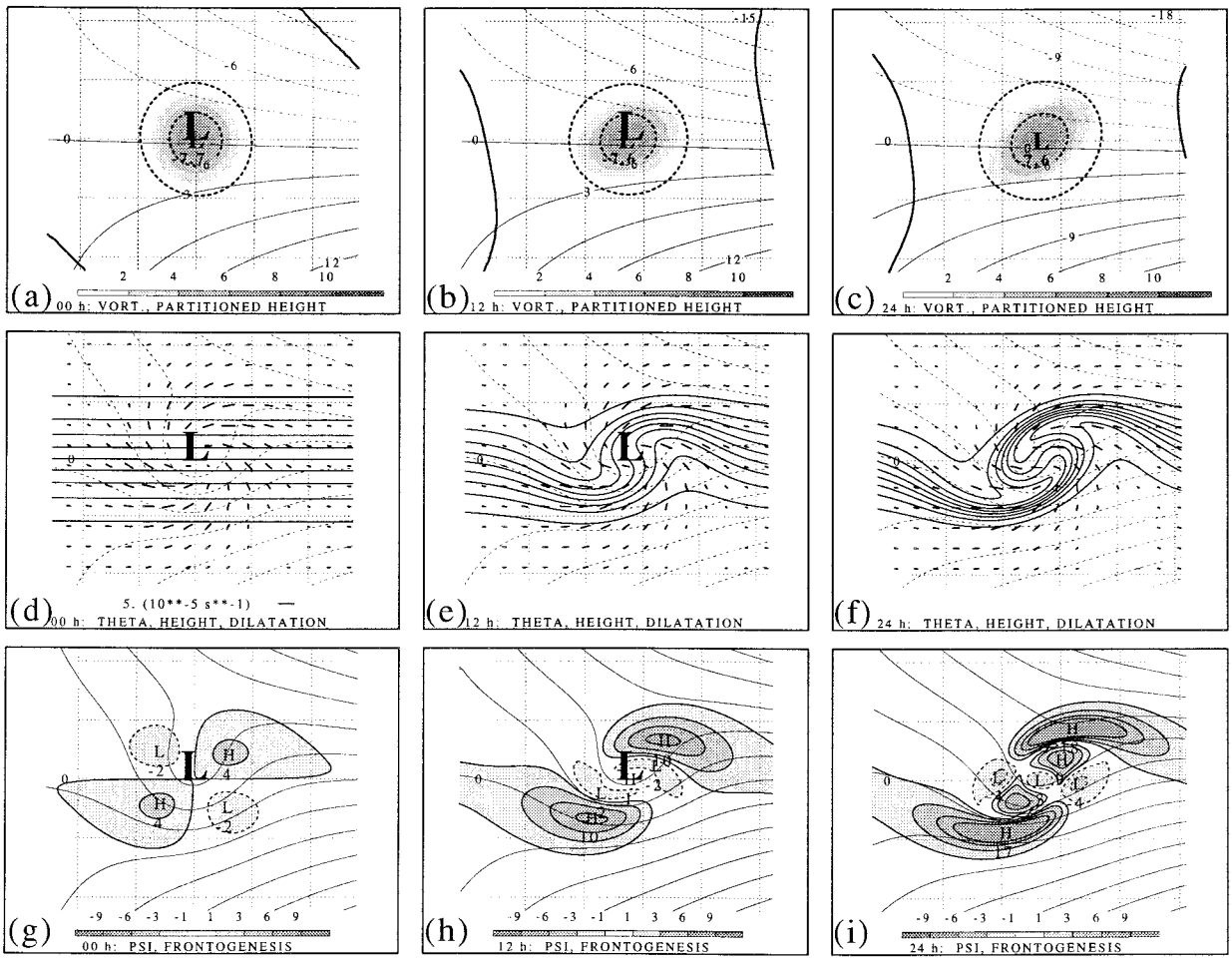

FIG. 14. As in Fig. 13 except for the circular Doswell vortex in confluent background flow (CONF).

clusion. One approach to simulating the role of advection of potential temperature by the divergent flow would be to employ baroclinic-model simulations of these vortices. For example, experiments with developing cyclones in background diffluence in a primitive equation model (H. Wernli 1996, personal communication) appear to support our hypothesis that divergence, along with deformation, acts to narrow the thermal ridge, producing an occluded front.

2) CIRCULAR DOSWELL VORTEX IN CONFLUENCE (CONF)

The addition of background confluent flow to the control case produces the simulation hereafter known as CONF (Fig. 14). The background confluence leads to zonal elongation and rotation of the vortex, which develops a southwest–northeast orientation by 24 h (Figs. 14a–c). The evolution of the vorticity in DIFF is similar to that in CONF except for a 90° rotation (cf. Figs. 13a–c and 14a–c), the same angle as that between the axes of dilatation of the background flows in DIFF and CONF. The dilatation axes in CONF approach those of the background flow (zonally oriented) away from the influence of the deformation associated with the vortex (Fig. 14d). Because of the large-scale confluence in the background flow, the largest deformation and frontogenesis at the initial time are southwest and northeast of the vortex center (Figs. 14d,g). By 12 h, these two regions of frontogenesis increase in area and magnitude, and they become more zonally elongated, separated by a large area composed of two frontolysis maxima (Fig. 14h) in a manner similar to the frontal-fracture area of IOP8 and the Shapiro–Keyser model (Figs. 7b and 10b). Consistent with the evolution of the frontogenesis patterns, zonally elongated cold and warm fronts form in CONF, separated by a relatively large region of weak potential temperature gradient (Fig. 14e). This evolution differs from that of DIFF, which features meridionally elongated fronts and a smaller area of frontolysis at the vortex center (cf. Figs. 14e,h and 13e,h). Also, in a manner similar to IOP8, the warm and cold fronts in CONF extend to the northeast and southwest of the vortex center, respectively (cf. Figs. 7b and 14e,h). Note

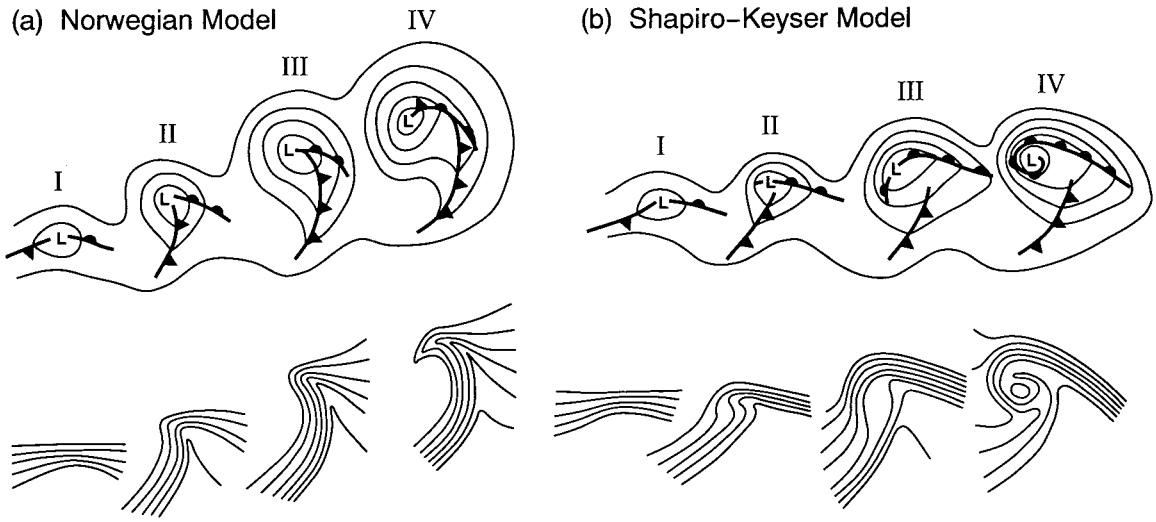

FIG. 15. Conceptual models of cyclone evolution showing lower-tropospheric (e.g., 850-hPa) geopotential height and fronts (top), and lower-tropospheric potential temperature (bottom). (a) Norwegian cyclone model: (I) incipient frontal cyclone, (II) and (III) narrowing warm sector, (IV) occlusion; (b) Shapiro–Keyser cyclone model: (I) incipient frontal cyclone, (II) frontal fracture, (III) frontal T-bone and bent-back front, (IV) frontal T-bone and warm seclusion. Panel (b) is adapted from Shapiro and Keyser (1990, their Fig. 10.27) to enhance the zonal elongation of the cyclone and fronts and to reflect the continued existence of the frontal T-bone in stage IV. The stages in the respective cyclone evolutions are separated by approximately 6–24 h and the frontal symbols are conventional. The characteristic scale of the cyclones based on the distance from the geopotential height minimum, denoted by L, to the outermost geopotential height contour in stage IV is 1000 km.

that the rotation of the isentropes into the northwest and southeast quadrants of the vortex within the first 12 h of CONF occurs much more slowly than that which occurs within the first 12 h of DIFF (cf. Figs. 14d,e and 13d,e), consistent with the slower frontal evolution of IOP8 compared to ATL1 (cf. Figs. 7a–c and 3a–c). At 24 h, the fronts in CONF continue to strengthen, exhibiting a well-defined T-bone configuration and bent-back front west of the vortex center (Fig. 14f,i), similar to IOP8 (Fig. 7b). Furthermore, the regions of frontolysis increase in magnitude and in areal coverage between 12 and 24 h (Figs. 14h,i), separating the cold and warm fronts by a much larger distance than in DIFF at 24 h (cf. Figs. 14f,i and Figs. 13f,i). Further integration of CONF (not shown) results in the lengthening of the bent-back front and the formation of a warm seclusion, consistent with the Shapiro–Keyser model.

In the idealized model simulations of DIFF and CONF, it might be asked whether the background deformation or the alteration of the initially circular vortex to a rotated and elongated configuration is primarily responsible for the differences in the resulting frontal structure and evolution. To test this hypothesis, a passive-tracer model with the same initial conditions as in DIFF and CONF was employed, but the total flow was specified to be steady. The results were qualitatively similar to those of DIFF and CONF (not shown), suggesting that the modifications to the flow arising from the rotation and elongation of the vortex play a secondary role in the frontal evolution.

5. Conclusions

In this paper, analyses of observed midlatitude oceanic cyclones and idealized simulations of vortices in a nondivergent barotropic model including background diffluence and confluence are presented, showing that the structure and evolution of cyclones and their attendant fronts are influenced by the large-scale flow in which they are embedded. In particular, two characteristic evolutions are examined, reminiscent of the Norwegian and Shapiro–Keyser cyclone models; these respective evolutions are illustrated schematically in Fig. 15.

The Norwegian cyclone model (Fig. 15a) typically applies to cyclones developing within diffluent, high-amplitude background flows, favoring the meridional elongation of the cyclone and its fronts. Initiation of cyclogenesis (I) occurs along a broad baroclinic zone. The cyclone develops a narrow, lengthy cold front, and a broad, short warm front (II). The strong poleward extension of the cold front (i.e., the absence of a frontal fracture) is attributed to the close proximity of the cold air arriving from the west toward the center of the cyclonic circulation, preventing the weakening of the potential temperature gradient in this area (Fig. 10a). The warm sector narrows as the cold front rotates toward the warm front, forming a thermal ridge characteristic of the Norwegian occluded front (III, IV). As the occlusion process continues, the baroclinicity along the warm front may become so diffuse that the cyclone may not appear to possess a well-defined warm front (IV).

This behavior is typical of cyclones at the end of storm tracks, as remarked by western United States and European meteorologists [e.g., the nonexistent warm front (Wallace and Hobbs 1977, 127; Friedman 1989, 217) or ''stubby'' warm front].

The Shapiro–Keyser cyclone model (Fig. 15b) typically applies to cyclones evolving within confluent, low-amplitude background flows. The cyclone begins as a weak disturbance on a slightly deformed baroclinic zone (I), as in the Norwegian cyclone model (stage I in Fig. 15a). While the cyclone deepens (II), the warm front intensifies and lengthens. Also at this time, the bent-back front first appears and a weakness in the potential temperature gradient develops along the poleward end of the cold front (i.e., the frontal fracture). A similar weakness occurs at the southwestward end of the developing bent-back front (Fig. 10b). The next phase of frontal development features the continued deepening of the cyclone and the elongation of the bent-back front (III). At its maximum intensity (IV), the Shapiro–Keyser cyclone develops a warm seclusion as cold air wraps around cool postfrontal air.

Idealizations of these two conceptual models of cyclone/frontal structure and evolution, consisting of an axisymmetric vortex embedded in diffluent and confluent background flows, were then simulated in a nondivergent barotropic model with potential temperature treated as a passive tracer. Specifically, when the vortex is placed in diffluent background flow, its frontal evolution resembles the Norwegian cyclone model with a dominant cold front and narrowing warm sector suggestive of the occlusion process. Alternatively, when the vortex is placed in confluent background flow, its frontal evolution resembles the Shapiro–Keyser model with a dominant warm front, frontal fracture, and frontal T-bone.

Considering the differences in the large-scale flow applicable to these respective conceptual models of cyclone/frontal structure and evolution, it is perhaps not surprising that the Norwegian model was formulated by Norwegian meteorologists analyzing cyclones in the high-amplitude, diffluent exit region of the North Atlantic storm track[8] and that the Shapiro–Keyser model was synthesized during ERICA, a field experiment that examined cyclones generally originating in the low-amplitude, confluent entrance region of the North Atlantic storm track. Although the transformation of some cyclones from one conceptual model to the other can occur (see section 3c), we suggest that these models represent two possible, yet distinct, members of a spectrum of types of observed cyclone evolution. Although this paper has not attempted to address the representativeness of these two conceptual models, since diffluence and confluence are typical of large-scale patterns associated with cyclogenesis [see, e.g., the conceptual models of cyclone life cycles presented by Evans et al. (1994) and Young (1995) for cyclogenesis in diffluent and confluent background flows], we are encouraged that our results likely possess some generality. In this regard, our results elucidating the relationship between the Norwegian and Shapiro–Keyser cyclone models and large-scale diffluence and confluence are confirmed by the recent work of M. Sinclair (1997, personal communication), who examined composite cyclone structures for cyclones over the western South Pacific Ocean using ECMWF analyses between 1990 and 1994. Furthermore, Sienkiewicz (1996) has found this relationship useful in the production of operational surface analyses at NCEP's Marine Prediction Center.

The results of this paper suggest that a single conceptual model (i.e., the Norwegian cyclone model) is insufficient to describe the frontal structure and evolution of the majority of midlatitude cyclones for the purpose of operational surface analysis. The inertia to maintain the Norwegian analysis methods may be due in part to the lack of a clearly superior, more versatile alternative. But any specific proposed alternative may be highly dependent on the regional cyclone environment and, therefore, may be limited in its global applicability (as discussed for the Norwegian cyclone model in section 1). This sentiment was stated previously by Sutcliffe (1952, 300), who argued that, ''although the [Norwegian] frontal model is sufficiently true to retain a permanent place in synoptic analysis . . . it must be allowed much freedom to fit the complexities of nature.'' Instead of trying to develop an all-encompassing conceptual model, perhaps attention should be directed toward more detailed understanding of the processes (e.g., the large-scale flow, surface friction, diabatic heating, physiographic forcing) that influence cyclone/frontal structure and evolution in various geographic settings. Then the variety of conceptual models in existence (e.g., the Norwegian and Shapiro–Keyser cyclone models) could be placed within the context of a spectrum of possible structures. This alternative might prove to be more satisfactory than developing a single, yet possibly cumbersome, conceptual model applicable to the majority of midlatitude cyclones.

Acknowledgments. This research is based on the first author's Ph.D. dissertation. We are deeply indebted to the following individuals for their contributions to this work: Prof. Gary Lackmann and Dr. Haig Iskenderian for assistance in obtaining ECMWF analyses; Prof. Lackmann for providing the Lanczos filter; Prof. Roger Smith and Dr. Wolfgang Ulrich for providing their barotropic model; Phil Cunningham and Dr. Greg Hakim for offering advice on the implementation of the barotropic model; Prof. Jim Steenburgh for suggesting the Godske et al. (1957) reference to the frontal fracture and his interest in this research; Prof. Cliff Mass for

[8] The location and dynamics of the North Atlantic storm track are discussed by, for example, Blackmon et al. (1977), Wallace et al. (1988), Hoskins and Valdes (1990), and Ayrault et al. (1995).

discussing these ideas in their formative stages; Prof. Stephen Mudrick, Dr. Heinrich Wernli, and Dr. Mark Sinclair for sharing their unpublished research results; Dr. Charles Doswell III, Dr. David Knight, and Prof. John Molinari for serving on the first author's dissertation committee and providing comments that improved the content and presentation of this work; Drs. William Thompson, Jeff Whitaker, and Doswell, and an anonymous reviewer for commenting on earlier versions of this manuscript; and Joan O'Bannon for drafting Figs. 10 and 15.

We are grateful to ECMWF and the Scientific Computing Division of NCAR for providing the data and a portion of the computing resources used in this study. This research was supported by the National Science Foundation through Grants ATM-9114598, ATM-9114743, ATM-9413012, and ATM-9421678, awarded to The University at Albany, State University of New York. The publication of this research was completed while the first author was a National Research Council Postdoctoral Research Associate at the National Severe Storms Laboratory.

REFERENCES

Ayrault, F., F. Lalaurette, A. Joly, and C. Loo, 1995: North Atlantic ultra high frequency variability: An introductory survey. *Tellus,* **47A,** 671–696.

Bergeron, T., 1928: Über die dreidimensional verknüpfende Wetteranalyse I. *Geofys. Publ.,* **5** (6), 1–111.

——, 1937: On the physics of fronts. *Bull. Amer. Meteor. Soc.,* **18,** 265–275.

——, 1959: Methods in scientific weather analysis and forecasting: An outline in the history of ideas and hints at a program. *The Atmosphere and Sea in Motion: Scientific Contributions to the Rossby Memorial Volume,* B. Bolin, Ed., Rockefeller Institute Press, 440–474.

Bishop, C. H., 1996: Domain-independent attribution. Part II: Its value in the verification of dynamical theories of frontal waves and frontogenesis. *J. Atmos. Sci.,* **53,** 253–262.

Bjerknes, J., 1919: On the structure of moving cyclones. *Geofys. Publ.,* **1** (2), 1–8.

——, 1930: Practical examples of polar-front analysis over the British Isles in 1925–6. *Geophys. Mem.,* **5** (10), 1–21 and 28 pp. of figures.

——, and H. Solberg, 1922: Life cycle of cyclones and the polar front theory of atmospheric circulation. *Geofys. Publ.,* **3** (1), 3–18.

Blackmon, M. L., J. M. Wallace, N.-C. Lau, and S. L. Mullen, 1977: An observational study of the Northern Hemisphere wintertime circulation. *J. Atmos. Sci.,* **34,** 1040–1053.

Blier, W., and R. M. Wakimoto, 1995: Observations of the early evolution of an explosive oceanic cyclone during ERICA IOP 5. Part I: Synoptic overview and mesoscale frontal structure. *Mon. Wea. Rev.,* **123,** 1288–1310.

Bosart, L. F., 1998: Observed cyclone life cycles. *The Life Cycles of Extratropical Cyclones,* M. A. Shapiro and S. Grønås, Eds., in press.

——, G. J. Hakim, K. R. Tyle, M. A. Bedrick, W. E. Bracken, M. J. Dickinson, and D. M. Schultz, 1996: Large-scale antecedent conditions associated with the 12–14 March 1993 cyclone (''Superstorm '93'') over eastern North America. *Mon. Wea. Rev.,* **124,** 1865–1891.

Browning, K. A., 1990: Organization of clouds and precipitation in extratropical cyclones. *Extratropical Cyclones, The Erik Palmén Memorial Volume,* C. W. Newton and E. O. Holopainen, Eds., Amer. Meteor. Soc., 129–153.

Brunt, D., 1934: *Physical and Dynamical Meteorology.* Cambridge University Press, 411 pp.

Cammas, J.-P., and D. Ramond, 1989: Analysis and diagnosis of the composition of ageostrophic circulations in jet-front systems. *Mon. Wea. Rev.,* **117,** 2447–2462.

Carlson, T. N., 1991: *Mid-Latitude Weather Systems.* Harper Collins, 507 pp.

Chan, J. C. L., and R. T. Williams, 1987: Analytical and numerical studies of the beta-effect in tropical cyclone motion. Part I: Zero mean flow. *J. Atmos. Sci.,* **44,** 1257–1265.

Cressman, G., 1985: The ''Reichelderfer papers.'' *Bull. Amer. Meteor. Soc.,* **66,** 1425–1426.

Davies, H. C., C. Schär, and H. Wernli, 1991: The palette of fronts and cyclones within a baroclinic wave development. *J. Atmos. Sci.,* **48,** 1666–1689.

Davies-Jones, R., 1985: Comments on ''A kinematic analysis of frontogenesis associated with a nondivergent vortex.'' *J. Atmos. Sci.,* **42,** 2073–2075.

Doswell, C. A. III, 1984: A kinematic analysis of frontogenesis associated with a nondivergent vortex. *J. Atmos. Sci.,* **41,** 1242–1248.

——, 1985: Reply. *J. Atmos. Sci.,* **42,** 2076–2079.

Duchon, C. E., 1979: Lanczos filtering in one and two dimensions. *J. Appl. Meteor.,* **18,** 1016–1022.

Eady, E. T., 1949: Long waves and cyclone waves. *Tellus,* **1** (3), 33–52.

Eliassen, A., 1994: Vilhelm Bjerknes's early studies of atmospheric motions and their connection with the cyclone model of the Bergen School. *Vol. I, Proc. Int. Symp. on the Life Cycles of Extratropical Cyclones,* Bergen, Norway, Geophysical Institute, University of Bergen, Norway, 3–12.

Evans, M. S., D. Keyser, L. F. Bosart, and G. M. Lackmann, 1994: A satellite-derived classification scheme for rapid maritime cyclogenesis. *Mon. Wea. Rev.,* **122,** 1381–1416.

Friedman, R. M., 1989: *Appropriating the Weather: Vilhelm Bjerknes and the Construction of a Modern Meteorology.* Cornell University Press, 251 pp.

Godske, C. L., T. Bergeron, J. Bjerknes, and R. C. Bundgaard, 1957: *Dynamic Meteorology and Weather Forecasting.* Amer. Meteor. Soc., 800 pp.

Guinn, T. A., and W. H. Schubert, 1993: Hurricane spiral bands. *J. Atmos. Sci.,* **50,** 3380–3403.

Hadlock, R., and C. W. Kreitzberg, 1988: The Experiment on Rapidly Intensifying Cyclones over the Atlantic (ERICA) field study: Objectives and plans. *Bull. Amer. Meteor. Soc.,* **69,** 1309–1320.

Hartmann, D. L., 1995: A PV view of zonal flow vacillation. *J. Atmos. Sci.,* **52,** 2561–2576.

Hartnett, E., G. Forbes, and R. Hadlock, 1989: ERICA Field Phase Summary. ERICA Data Center, Department of Physics and Atmospheric Science, Drexel University. [Available from ERICA Data Center, Dept. of Physics and Atmospheric Science, Drexel University, Philadelphia, PA 19104.]

Hines, K. M., and C. R. Mechoso, 1993: Influence of surface drag on the evolution of fronts. *Mon. Wea. Rev.,* **121,** 1152–1175.

Hobbs, P. V., J. D. Locatelli, and J. E. Martin, 1990: Cold fronts aloft and the forecasting of precipitation and severe weather east of the Rocky Mountains. *Wea. Forecasting,* **5,** 613–626.

——, ——, and ——, 1996: A new conceptual model for cyclones generated in the lee of the Rocky Mountains. *Bull. Amer. Meteor. Soc.,* **77,** 1169–1178.

Hoffman, E. G., 1995: Evolution and mesoscale structure of fronts in the western United States: A case study. M.S. thesis, Dept. of Atmospheric Science, The University at Albany, State University of New York, 287 pp. [Available from Dept. of Atmospheric Science, The University at Albany, State University of New York, Albany, NY 12222.]

Hopfinger, E. J., and G. J. F. van Heijst, 1993: Vortices in rotating fluids. *Annu. Rev. Fluid Mech.,* **25,** 241–289.

Hoskins, B. J., 1983: Dynamical processes in the atmosphere and the use of models. *Quart. J. Roy. Meteor. Soc.,* **109,** 1–21.
——, 1990: Theory of extratropical cyclones. *Extratropical Cyclones, The Erik Palmén Memorial Volume,* C. W. Newton and E. O. Holopainen, Eds., Amer. Meteor. Soc., 63–80.
——, and F. P. Bretherton, 1972: Atmospheric frontogenesis models: Mathematical formulation and solution. *J. Atmos. Sci.,* **29,** 11–37.
——, and N. V. West, 1979: Baroclinic waves and frontogenesis. Part II: Uniform potential vorticity jet flows—Cold and warm fronts. *J. Atmos. Sci.,* **36,** 1663–1680.
——, and P. J. Valdes, 1990: On the existence of storm-tracks. *J. Atmos. Sci.,* **47,** 1854–1864.
Huschke, R. E., Ed., 1959: *Glossary of Meteorology.* Amer. Meteor. Soc., 638 pp.
James, I. N., 1987: Suppression of baroclinic instability in horizontally sheared flows. *J. Atmos. Sci.,* **44,** 3710–3720.
Jewell, R., 1981: Tor Bergeron's first year in the Bergen school: Towards an historical appreciation. *Weather and Weather Maps: A Volume Dedicated to the Memory of Tor Bergeron,* G. H. Liljequist, Ed., Contributions to Current Research in Geophysics, Vol. 10, Birkhäuser Verlag, 474–490.
Keyser, D., and M. J. Pecnick, 1985: A two-dimensional primitive equation model of frontogenesis forced by confluence and horizontal shear. *J. Atmos. Sci.,* **42,** 1259–1282.
——, M. J. Reeder, and R. J. Reed, 1988: A generalization of Petterssen's frontogenesis function and its relation to the forcing of vertical motion. *Mon. Wea. Rev.,* **116,** 762–780.
——, B. D. Schmidt, and D. G. Duffy, 1989: A technique for representing three-dimensional vertical circulations in baroclinic disturbances. *Mon. Wea. Rev.,* **117,** 2463–2494.
Koch, S. E., M. desJardins, and P. J. Kocin, 1983: An interactive Barnes objective map analysis scheme for use with satellite and conventional data. *J. Climate Appl. Meteor.,* **22,** 1487–1503.
Kuo, Y.-H., and S. Low-Nam, 1994: Effects of surface friction on the thermal structure of an extratropical cyclone. *Vol. III, Proc. Int. Symp. on the Life Cycles of Extratropical Cyclones,* Bergen, Norway, Geophysical Institute, University of Bergen, Norway, 129–134.
——, M. A. Shapiro, and E. G. Donall, 1991: The interaction between baroclinic and diabatic processes in a numerical simulation of a rapidly intensifying extratropical marine cyclone. *Mon. Wea. Rev.,* **119,** 368–384.
——, R. J. Reed, and S. Low-Nam, 1992: Thermal structure and airflow in a model simulation of an occluding marine cyclone. *Mon. Wea. Rev.,* **120,** 2280–2297.
Kutzbach, G., 1979: *The Thermal Theory of Cyclones.* Amer. Meteor. Soc., 255 pp.
Lackmann, G. M., D. Keyser, and L. F. Bosart, 1997: A characteristic life cycle of upper-tropospheric cyclogenetic precursors during the Experiment on Rapidly Intensifying Cyclones over the Atlantic (ERICA). *Mon. Wea. Rev.,* **125,** 2729–2758.
Lanczos, C., 1956: *Applied Analysis.* Prentice-Hall, 539 pp.
Loughe, A. F., C.-C. Lai, and D. Keyser, 1995: A technique for diagnosing three-dimensional ageostrophic circulations in baroclinic disturbances on limited-area domains. *Mon. Wea. Rev.,* **123,** 1476–1504.
Mass, C., 1991: Synoptic frontal analysis: Time for a reassessment? *Bull. Amer. Meteor. Soc.,* **72,** 348–363.
——, and D. M. Schultz, 1993: The structure and evolution of a simulated midlatitude cyclone over land. *Mon. Wea. Rev.,* **121,** 889–917.
Melander, M. V., J. C. McWilliams, and N. J. Zabusky, 1987: Axisymmetrization and vorticity-gradient intensification of an isolated two-dimensional vortex through filamentation. *J. Fluid Mech.,* **178,** 137–159.
Namias, J., 1950: The index cycle and its role in the general circulation. *J. Meteor.,* **7,** 130–139.
——, 1983: The history of polar front and air mass concepts in the United States—An eyewitness account. *Bull. Amer. Meteor. Soc.,* **64,** 734–755.
Neiman, P. J., and M. A. Shapiro, 1993: The life cycle of an extratropical marine cyclone. Part I: Frontal-cyclone evolution and thermodynamic air–sea interaction. *Mon. Wea. Rev.,* **121,** 2153–2176.
Newton, C., and H. Rodebush Newton, 1994: The Bergen School concepts come to America. *Vol. I, Proc. Int. Symp. on the Life Cycles of Extratropical Cyclones,* Bergen, Norway, Geophysical Institute, University of Bergen, Norway, 22–31.
Nuss, W. A., and R. A. Anthes, 1987: A numerical investigation of low-level processes in rapid cyclogenesis. *Mon. Wea. Rev.,* **115,** 2728–2743.
Orlanski, I., 1975: Rational subdivision of scales for atmospheric processes. *Bull. Amer. Meteor. Soc.,* **56,** 527–530.
——, and J. P. Sheldon, 1995: Stages in the energetics of baroclinic systems. *Tellus,* **47A,** 605–628.
Palmén, E., and C. W. Newton, 1969: *Atmospheric Circulation Systems.* Academic Press, 603 pp.
Petterssen, S., 1936: Contribution to the theory of frontogenesis. *Geofys. Publ.,* **11** (6), 1–27.
——, 1956: *Weather Analysis and Forecasting. Vol. I, Motion and Motion Systems.* 2d ed. McGraw-Hill, 428 pp.
——, and S. J. Smebye, 1971: On the development of extratropical cyclones. *Quart. J. Roy. Meteor. Soc.,* **97,** 457–482.
——, D. L. Bradbury, and K. Pedersen, 1962: The Norwegian cyclone models in relation to heat and cold sources. *Geofys. Publ.,* **24** (9), 243–280.
Reed, R. J., Y.-H. Kuo, and S. Low-Nam, 1994: An adiabatic simulation of the ERICA IOP 4 storm: An example of quasi-ideal frontal cyclone development. *Mon. Wea. Rev.,* **122,** 2688–2708.
Reichelderfer, F. W., 1932: Norwegian methods of weather analysis. Unpublished notes (see Cressman 1985), 45 pp.
Ross, S., 1984: *A First Course in Probability.* 2d ed. MacMillan, 392 pp.
Rossby, C.-G., and Collaborators, 1939: Relation between variations in the intensity of the zonal circulation of the atmosphere and the displacements of the semipermanent centers of action. *J. Mar. Res.,* **2,** 38–55.
——, and H. C. Willett, 1948: The circulation of the upper troposphere and lower stratosphere. *Science,* **108,** 643–652.
Rotunno, R., W. C. Skamarock, and C. Snyder, 1996: High-resolution simulations of idealized baroclinic waves with and without surface drag. Preprints, *Seventh Conf. on Mesoscale Processes,* Reading, United Kingdom, Amer. Meteor. Soc., 6–8.
Saucier, W. J., 1955: *Principles of Meteorological Analysis.* The University of Chicago Press, 438 pp.
Sawyer, J. S., 1950: Formation of secondary depressions in relation to the thickness pattern. *Meteor. Mag.,* **79,** 1–5.
Schultz, D. M., 1996: The effect of large-scale flow on low-level frontal structure and evolution in midlatitude oceanic cyclones. Ph.D. dissertation, The University at Albany, State University of New York, 192 pp. [Available from Dept. of Atmospheric Science, The University at Albany, State University of New York, Albany, NY 12222.]
——, and C. F. Mass, 1993: The occlusion process in a midlatitude cyclone over land. *Mon. Wea. Rev.,* **121,** 918–940.
——, W. E. Bracken, L. F. Bosart, G. J. Hakim, M. A. Bedrick, M. J. Dickinson, and K. R. Tyle, 1997: The 1993 Superstorm cold surge: Frontal structure, gap flow, and tropical impact. *Mon. Wea. Rev.,* **125,** 5–39; Corrigendum. *Mon. Wea. Rev.,* **125,** 662.
Shapiro, M. A., and D. Keyser, 1990: Fronts, jet streams and the tropopause. *Extratropical Cyclones, The Erik Palmén Memorial Volume,* C. W. Newton and E. O. Holopainen, Eds., Amer. Meteor. Soc., 167–191.
——, and E. Donall Grell, 1994: In search of synoptic/dynamic conceptualizations of the life cycles of fronts, jet streams, and the tropopause. *Vol. I, Proc. Int. Symp. on the Life Cycles of Extratropical Cyclones,* Bergen, Norway, Geophysical Institute, University of Bergen, Norway, 163–181.

Sienkiewicz, J. M., 1996: Surface analysis at NCEP's Marine Prediction Center. Preprints, *15th Conf. on Weather Analysis and Forecasting,* Norfolk, VA, Amer. Meteor. Soc., 487–490.

Smigielski, F. J., and H. M. Mogil, 1995: A systematic satellite approach for estimating central surface pressures of mid-latitude cold season oceanic cyclones. *Tellus,* **47A,** 876–891.

Smith, R. K., W. Ulrich, and G. Dietachmayer, 1990: A numerical study of tropical cyclone motion using a barotropic model. I: The role of vortex asymmetries. *Quart. J. Roy. Meteor. Soc.,* **116,** 337–362.

Steenburgh, W. J., and C. F. Mass, 1994: The structure and evolution of a simulated Rocky Mountain lee trough. *Mon. Wea. Rev.,* **122,** 2740–2761.

Sutcliffe, R. C., 1952: Principles of weather forecasting. *Quart. J. Roy. Meteor. Soc.,* **78,** 291–320.

Takayabu, I., 1986: Roles of the horizontal advection on the formation of surface fronts and on the occlusion of a cyclone developing in the baroclinic westerly jet. *J. Meteor. Soc. Japan,* **64,** 329–345.

Thompson, W. T., 1995: Numerical simulations of the life cycle of a baroclinic wave. *Tellus,* **47A,** 722–732.

Thorncroft, C. D., B. J. Hoskins, and M. E. McIntyre, 1993: Two paradigms of baroclinic-wave life-cycle behavior. *Quart. J. Roy. Meteor. Soc.,* **119,** 17–55.

Tibaldi, S., A. Buzzi, and A. Speranza, 1990: Orographic cyclogenesis. *Extratropical Cyclones, The Erik Palmén Memorial Volume,* C. W. Newton and E. O. Holopainen, Eds., Amer. Meteor. Soc., 107–127.

Trenberth, K. E., 1992: Global analyses from ECMWF and atlas of 1000 to 10 mb circulation statistics. NCAR Tech. Note NCAR/TN-373+STR, 191 pp.

Uccellini, L. W., S. F. Corfidi, N. W. Junker, P. J. Kocin, and D. A. Olson, 1992: Report on the surface analysis workshop held at the National Meteorological Center 25–28 March 1991. *Bull. Amer. Meteor. Soc.,* **73,** 459–472.

Vederman, J., 1954: The life cycles of jet streams and extratropical cyclones. *Bull. Amer. Meteor. Soc.,* **35,** 239–244.

Wallace, J. M., and P. V. Hobbs, 1977: *Atmospheric Science: An Introductory Survey.* Academic Press, 467 pp.

——, G.-H. Lim, and M. L. Blackmon, 1988: Relationship between cyclone tracks, anticyclone tracks and baroclinic waveguides. *J. Atmos. Sci.,* **45,** 439–462.

Wernli, J. H., 1995: Lagrangian perspective of extratropical cyclogenesis. Dissertation No. 11016, Swiss Federal Institute of Technology, 157 pp. [Available from H. Wernli, Atmospheric Physics, ETH Hönggerberg, CH-8093, Zurich, Switzerland.]

——, and H. C. Davies, 1997: A Lagrangian-based analysis of extratropical cyclones. Part I: The method and some applications. *Quart. J. Roy. Meteor. Soc.,* **123,** 467–489.

Young, M. V., 1995: Types of cyclogenesis. *Images in Weather Forecasting,* M. J. Bader, G. S. Forbes, J. R. Grant, R. B. E. Lilley, and A. J. Waters, Eds., Cambridge University Press, 213–286.